Draft version February 2, 2022
Typeset using LaTeX default style in AASTeX631

Mars Climate Sounder observations of gravity wave activity throughout Mars's lower atmosphere

Nicholas G. Heavens [1,2] Alexey Pankine [1] J. Michael Battalio [3] Corwin Wright [4] David M. Kass [5] Armin Kleinböhl [5] Sylvain Piqueux [5] and John T. Schofield [5,*]

[1] Space Science Institute, 4765 Walnut St, Suite B, Boulder, CO 80301
[2] Department of Earth Science and Engineering, Imperial College, London, UK
[3] Department of Earth and Planetary Sciences, Yale University, New Haven, CT, USA
[4] Centre for Space, Atmospheric and Oceanic Science, University of Bath, Bath, UK
[5] NASA Jet Propulsion Laboratory, California Institute of Technology, Pasadena, CA, USA

(Received 1 November 2021; Revised 19 January 2022; Accepted 2 February 2022)

Submitted to PSJ

ABSTRACT

Gravity waves are one way Mars's lower atmospheric weather can affect the circulation and even composition of Mars's middle and upper atmosphere. A recent study showed how on-planet observations near the center of the 15 micron CO_2 band by the A3 channel **(635–665 cm^{-1})** of the Mars Climate Sounder on board Mars Reconnaissance Orbiter (MRO-MCS) could sense horizontally short, vertically broad gravity waves at $\approx$ 25 km above the surface by looking at small-scale radiance variability in temperature-sensitive channels. This approach is extended here to two additional channels closer to the wings of the 15 micron CO_2 band, **A1 (595–615 cm^{-1}) and A2 (615–645 cm^{-1})**, to sense gravity waves throughout the lower atmosphere. Using information from all three channels demonstrates that gravity wave activity in Mars's lowermost atmosphere is dominated by orographic sources, particularly over the extremely rough terrain of Valles Marineris. Much of this orographic population is either trapped or filtered in the lowest two scale heights, such that variations in filtering and non-orographic sources shape the gravity wave population observed at 25 km above the surface. During global dust storms, however, gravity wave activity in the first scale height decreases by approximately a factor of two, yet trapping/filtering of what activity remains in the tropics substantially weakens. Exceptionally high radiance variability at night in the tropics during the less dusty part of the year is the result of observing mesospheric clouds rather than gravity waves.

Keywords: Mars (1007), Planetary atmospheres (1244), Atmospheric variability (2119)

1. INTRODUCTION

In a planetary atmosphere, disturbances in a stably stratified fluid can be restored by buoyancy, resulting in the formation of an atmospheric gravity wave (GW) (Fritts & Alexander 2003). GW can propagate vertically through the atmosphere and become unstable, transporting energy and momentum from lower to higher levels of the atmosphere (e.g., Holton et al. 1995; Yamanaka 1995; Yiğit & Medvedev 2015; Medvedev & Yiğit 2019). GW activity in the atmospheres of the Earth and Mars can have a variety of analogous dynamical consequences, including the closure of middle atmospheric jets (e.g., Holton 1982; Barnes 1990; Medvedev et al. 2011), the formation of middle atmospheric clouds under otherwise unfavorable thermodynamical conditions (e.g., Fritts et al. 1993; Spiga et al. 2012), and the setting of the vertical extent of the homosphere (homopause altitude) (e.g., Offermann et al. 2006; Slipski et al. 2018).

Corresponding author: Nicholas G. Heavens
nheavens@spacescience.org

* Retired

In the case of Mars, turbulence generated by GW breaking enhances mixing at middle to upper atmospheric altitudes (70–140 km) where eddy diffusion is otherwise weakening (Slipski et al. 2018).

The potential impact of GW activity on homopause altitude suggests understanding GW activity is not only necessary for understanding the behavior of the present day atmosphere but **also for** understanding the evolution of Mars's atmospheric composition through time. As noted by Slipski et al. (2018), an atmosphere with a higher homopause, i.e., one in which atmospheric gases are well-mixed to higher altitude, is one in which escaping species are less isotopically fractionated. In addition, GW in the upper atmosphere strongly affect exospheric temperatures locally and possibly enhance atmospheric escape (Parish et al. 2009; Walterscheid et al. 2013; England et al. 2017; Williamson et al. 2019; Leelavathi et al. 2020; Yiğit et al. 2020).

GW activity in the upper atmosphere is diurnally and seasonally variable. It is strongest on average during southern spring afternoons, possibly because of strong dust storm activity during that season (Liu et al. 2019). However, the relationship between upper atmospheric GW activity and dust storm activity is complicated by the effects dust storms can have on the density structure of the thermosphere (Liu et al. 2019). Nevertheless, there is independent evidence that the global dust storms of 2001 and 2018 significantly raised the altitude below which Mars's atmospheric composition was dominated by higher molecular mass CO_2 as opposed to lower molecular mass O (Xu et al. 2015; Elrod et al. 2020). **(The dust storms of 2001 and 2018 will be referred to hereafter as 25P and 34P, because they occurred in Mars Years 25 and 34 in the sense of Clancy et al. (2000); Piqueux et al. (2015a)).** Mars's well-mixed atmospheric composition is dominated by CO_2, so CO_2 dominance at higher altitude implies a higher homopause altitude, and thus potentially breaking of GW at higher altitude, a type of seasonal variability observed by Liu et al. (2019) and reported in 34P by Elrod et al. (2019). In addition, Leelavathi et al. (2020); Yiğit et al. (2020) recently have shown that upper atmospheric gravity wave amplitudes increased by a factor of 2 or more during 34P, despite the high likelihood that gravity waves would be more strongly filtered by convective instability in the warmer conditions near 100 km that prevailed during 34P (England et al. 2017; Vals et al. 2019; Leelavathi et al. 2020; Yiğit et al. 2020).

One pathway to understanding variability in upper atmospheric GW activity is to study the observational record of GW activity in the lower and middle atmosphere. Because of various dissipative processes and the possible production of secondary GW during breaking (e.g., Vadas & Fritts 2001; Chun & Kim 2008; Vadas et al. 2018; Heale et al. 2020), the upper atmospheric GW population can be very different from what is observed in the lower and middle atmosphere. Nevertheless, observing the lower and middle atmospheric GW population is necessary to accurately predict the upper atmospheric population from first principles as well as to simulate the effects of GW through the whole atmosphere, because this population is ultimately what is being dissipated and forming secondary GW (e.g., Medvedev et al. 2011; Yiğit et al. 2015; Imamura et al. 2016; Kuroda et al. 2016, 2019; Gilli et al. 2020).

Recently, Heavens et al. (2020) argued that the observational record of lower and middle atmospheric GW activity at Mars could be vastly expanded by using small-scale variability in infrared observations sensitive to temperature as a proxy for GW activity. As reviewed by Heavens et al. (2020), previous studies of GW activity in the lower and middle atmosphere had been based on relatively infrequent occultation-type measurements (e.g., Creasey et al. 2006; Altieri et al. 2012), so leveraging the high frequency of measurements by mapping instruments like the Thermal Emission Spectrometer (TES) on board Mars Global Surveyor (MGS) or the Mars Climate Sounder (MCS) on board Mars Reconnaissance Orbiter (MRO) could have major advantages over radio occultation, **even if there were no difficulty in distinguishing tidal from GW oscillations in radio occultation profiles.**

Heavens et al. (2020) also provided a proof of concept of this idea by analyzing the variance in calibrated radiance (expressed as brightness temperature) in the MRO-MCS A3 channel (635–665 cm^{-1}: near the center of the 15 μm CO_2 band) in nadir geometry and in an "off-nadir" geometry, in which the surface was viewed at emission angles of $\approx 70°$. **MRO-MCS was designed to scan the limb as well as observe the surface with a detector array divided into lines of 21 detectors corrresponding to an individual channel (McCleese et al. 2007). In the limb, these 21 detectors observe the atmosphere from the side at a vertical resolution of 5 km, where detector 1 is at the top and detector 21 is at the bottom. In nadir geometry, these detectors observe the surface at a horizontal resolution near 1 km, with detector 1 being most forward in the direction of spacecraft motion and detector 21 being farthest aft. In the typical off-nadir geometry, the horizontal resolution stretches to $\approx$ 2.9 km (Hayne et al. 2012). Off-nadir observations from MRO-MCS**

far outnumber nadir observations because of elevation actuator problems after the first three months of science operations, which prevented MRO-MCS from regularly scanning to nadir thereafter (Jau & Kass 2008). Off-nadir views **in A3** were simulated to capture GW activity at ≈ 25 km above the surface, **and nadir views were simulated to capture GW activity 5 km lower**. Simulations suggested that the nadir views were sensitive to GW with horizontal wavelengths of 10–30 km and vertical wavelengths no less than 35 km, while the off-nadir views were sensitive to GW with horizontal wavelengths of 10–100 km and vertical wavelengths around half of the corresponding horizontal wavelength.

However, these simulations were based on a parameterization of the A3 vertical weighting function in off-nadir geometry derived from the calculated nadir weighting function and did not consider possible changes to the vertical weighting function under high dust opacity conditions. Incorrectly estimating the off-nadir weighting function under clear conditions risks incorrect assessment of the vertical wavelength of the observed GW and incorrect estimate of their propagation potential into the thermosphere. Imamura et al. (2016) suggested that GW with vertical wavelengths < 20 km would be strongly filtered during the transition between the middle and upper atmosphere, which is somewhat supported by the finding of Siddle et al. (2019) that the dominant vertical wavelength in the thermosphere is ≈ 20 km. Neglecting changes in vertical weighting function under high dust opacity conditions risks misinterpreting the altitude to which the GW observations are sensitive, which could result in mistaking changes in the altitude of sensitivity for changes in GW activity where GW dissipation is strong.

From analyzing brightness temperature variances in on-planet observations in the A3 channel, Heavens et al. (2020) concluded that: (1) strong GW activity followed the winter westerly jets in the extratropics and tropical easterly jet over the Tharsis volcanoes; (2) GW activity in areas of climatologically low–moderate GW activity strongly decreased during regional and global dust storms (contradicting the inference from the upper atmospheric GW observations but also raising questions about the effect of dust on the vertical weighting function); and (3) strong but infrequent nighttime GW activity appears to be high in some parts of the tropics during much of the year, which could indicate either a significant GW source there, such as convective water ice clouds driven by radiative cooling (Spiga et al. 2017) or else contamination of the analysis by re-emission of radiation by CO_2 clouds in the middle atmosphere.

An additional, yet unhighlighted point that could be drawn from the analysis of Heavens et al. (2020) was the strong mismatch between the apparent distribution of GW activity and a "topographic hypothesis" based on the estimated wind stress. This aspect of the analysis recapitulated an argument made by Creasey et al. (2006) that if observed GW were orographically generated, their distribution should follow the global distribution of wind stress, which is strongest over Valles Marineris. Thus, GW activity at 25 km and, by extension, GW that reach the middle atmosphere (30–50 km altitude), are principally generated by non-orographic sources (presumably because GW from orographic sources are non-existent or have been strongly filtered).

The purpose of this study is to re-assess the multiannual record of GW activity presented by Heavens et al. (2020), focusing on the three areas of uncertainty outlined above rather than on all possible aspects of GW climatology that could be addressed with the data, i.e., (1) whether GW activity in the lower atmosphere increases or decreases during regional and global dust storm activity; (2) whether there is a strong source of GW activity in the nighttime tropics due to water ice cloud convection driven by radiative cooling; (3) whether GW activity appears to be controlled by non-orographic sources throughout the lower atmosphere. To make this re-assessment, we will analyze variance in nadir and off-nadir views by MRO-MCS in a broader range of channels that includes A3. The A1 (595-615 cm^{-1}) and A2 (615-645 cm^{-1}) channels in the wings of 15 μm CO_2 band will be analyzed to sense GW activity/mesoscale variability in the lower atmosphere below 25 km. As noted by Heavens et al. (2020), A1 and A2 are also more transparent to CO_2 ice than A3, so these channels might be able to be used to look for GW activity related to nighttime water ice cloud convection in the tropics without the ambiguity introduced by the presence of middle atmospheric CO_2 ice clouds.

The outline of this paper is as follows. In Section 2, the sensitivity of A1–A3 to GW activity under low and high dust conditions will be evaluated and the importance of the surface contribution to variance analysis over high elevation surfaces will be assessed. In Section 3, the analysis of the dataset and any other analyses necessary for its interpretation will be described. In Section 4, the results of the analysis that are relevant to the four areas of focus of the study will be presented. These results will be discussed in Section 5 and summarized in Section 6.

2. SENSITIVITY OF THE OBSERVATIONS TO GRAVITY WAVE ACTIVITY

2.1. *Visibility analysis*

GW propagate with different wavelengths and angles within a planetary atmosphere, which can be incompletely resolved by a remote sensing observation (Wu et al. 2006). This effect can be captured and quantified by simulating a quantity called visibility, which is the proportion of brightness temperature variance due to GW that is recovered by an observational method as a function of GW horizontal and vertical wavelength (Wu & Eckermann 2008). To calculate the visibility of gravity wave activity in channels A1–A3, the basic technique outlined by Heavens et al. (2020) was followed. Here, relevant details about the MRO-MCS observations will be provided in the proper place, but a more thorough account is provided by Heavens et al. (2020) and will not be fully recapitulated here.

2.1.1. *Radiative transfer modeling*

Radiative transfer modeling was used to calculate the vertical and horizontal weighting functions for nadir and off-nadir observations by MRO-MCS in the relevant channels. It was assumed that off-nadir observations were made at the typical angle of 8.9° below the limb, which corresponds to a surface emission angle of 67.04° **in the detector closest to the surface, 21, and 73.20° in the detector farthest from the surface, 1.** The surface contributions were estimated from the difference between the sum of the vertical weighting functions and unity.

These weighting function calculations were made for three input atmospheres, two of which were the Kliore (1978) standard atmospheres for the northern and southern hemispheres **(compiled under the auspices of the Committee on Space Research (COSPAR) and so often referred to as the COSPAR standard atmospheres)**, which were assumed to be clear of aerosol. The third atmosphere enabled calculation of the weighting functions under extreme aerosol conditions by adopting a profile from the Mars Climate Database for L_s=280° in the Martian Year 28 scenario at 45° S, 40° E at 15:00 LST (Millour et al. 2015; MCD cited 2018). This profile approximates conditions during the mature phase of 28P in the southern hemisphere. Total visible dust column optical depth in the profile is 2.69, which while on high end for this scenario and MCD scenarios in general, may significantly underestimate typical dust column opacities in global dust storms. The Mars Exploration Rovers, *Spirit* and *Opportunity*, measured maximum visible opacities near 5 during 28P, while the Mars Science Laboratory, Curiosity, measured a maximum visible opacity of ≈ 8 (Guzewich et al. 2019) in 34P. That said, unlike the rover observations or satellite observations that could potentially have been used to supplement them to build an input atmosphere, the MCD scenario provides a physically consistent temperature profile along with a dust profile over the entire atmospheric column, which is essential to the radiative transfer modeling.

Dust was incorporated into the radiative transfer modeling by assuming a 2 μm dust particle size with optical properties corresponding to those derived by Wolff & Clancy (2003). The resulting column optical depth in the dusty profile at 9.3 μm under these assumptions is 1.5.

The simulated A3 vertical weighting functions agree well with those previously simulated by Kleinböhl et al. (2010), which were used by Heavens et al. (2020) as the basis of their visibility calculations (Figs. 1a; 2c,f), particularly in the Northern Hemisphere. This close agreement enables confident assessment of the altitude to which each channel is most sensitive by looking at the peak of the vertical weighting function.

In the standard atmospheres, the nadir views peak at the surface in A1 (with a strong additional surface contribution of up to 40%, at 10 km in A2, and at 21 km in A3) (Figs. 1a–b). In dusty conditions, the altitude of peak sensitivity increases in all channels by 5–10 km because of the additional opacity from dust, so that A1's vertical weighting function under dusty conditions is similar to that of A2 under clear conditions, though A2's vertical weighting function does not rise enough to match A3's vertical weighting function under clear conditions (Figs. 1a–c).

Off-nadir vertical weighting functions for the lowest and highest detectors in off-nadir geometry slightly diverge at low and high altitudes but peak at nearly the same altitude ≈ 5 km above the corresponding vertical weighting function in the nadir. Surface contributions are smaller than the nadir by a factor of 2–3 in A1 and A2 but similar in A3. As in the nadir case, dusty conditions raise the peak altitude of sensitivity in the off-nadir, such that the A2 and A1 vertical weighting functions under dusty conditions approximate the A3 and A2 vertical weighting functions under clear conditions (Figs. 2a–i).

Thus, A1 will be most sensitive to near-surface variability in clearer conditions and variability at 15 km in dusty conditions; A2 will be most sensitive to variability at 15 km in clearer conditions and variability at 25 km in dusty conditions; A3 will be most sensitive to variability at 25 km in clearer conditions and variability at 30 km in dusty conditions.

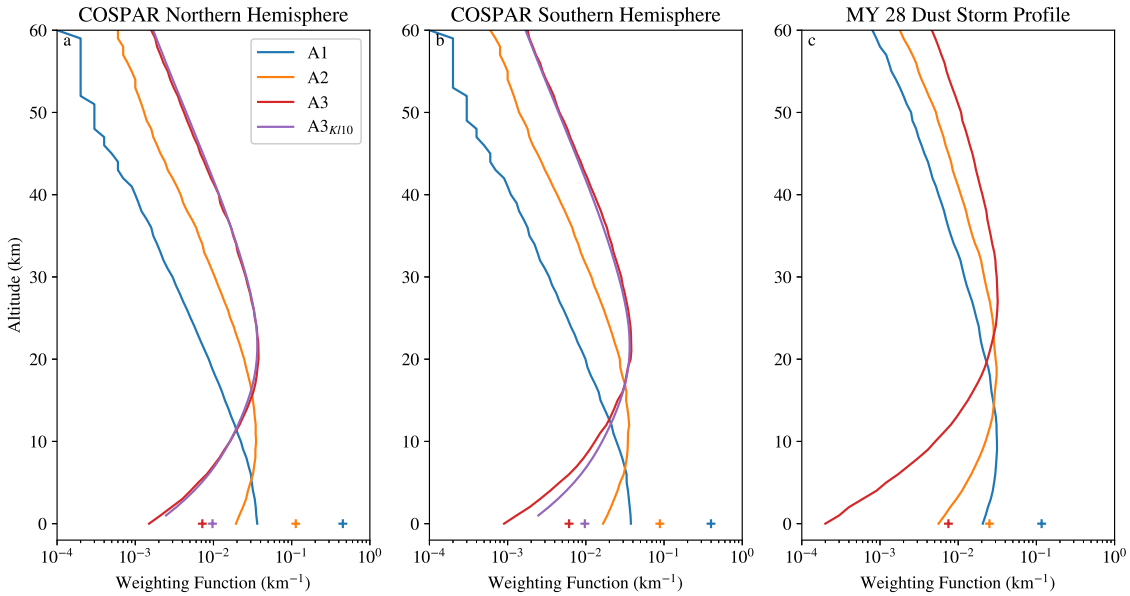

Figure 1. Comparison of the vertical weighting functions for the MRO-MCS A1–A3 channels and nadir geometry for the three input atmospheres, as labeled. The estimated surface contributions are marked with crosses at 0 km altitude in each panel. The weighting functions have been plotted over a more limited vertical range than calculated to emphasize the altitudes at which they peak. A3$_{Kl10}$ refers to the nadir weighting function for A3 calculated by Kleinböhl et al. (2010).

.

The horizontal weighting functions for the off-nadir observations show that off-nadir observations are capturing information over a 100–200 km range from the center of the observation at the surface (Figs. 3a–i). One consequence of this is that if a diagnosis of GW activity is assigned a position in space based on the intersection of detector 11's optical path with the surface **(the center of the line of 21 detectors)**, the true position of the measurement projected to the surface is actually 30–90 km closer to the sub-spacecraft point than assumed.

Unlike weighting functions in nadir geometry, those in off-nadir geometry are slanted, which is easily illustrated by constructing two-dimensional weighting functions for nadir and off-nadir views in an x-z plane of 1000 × 100 km, binned at 1 km resolution (Figs. 4a–b). The surface contribution was added to the lowest level of the vertical weighting function. The vertical weighting functions were then distributed across bins to account for the width of the off-nadir optical path (≈ 3 km) and smearing of each measurement by spacecraft motion during each 2.048 s measurement (≈ 6 km), and then re-normalized to sum to unity. Two-dimensional weighting functions like this were constructed for each channel, detector, and atmosphere.

2.1.2. *GW-perturbed model atmospheres*

To evaluate the sensitivity of the GW diagnosis technique, GW-perturbed model atmospheres were constructed over the same x-z domain as the two-dimensional weighting functions corresponding to the three model atmospheres used to calculate the weighting functions. In other words, the unperturbed atmospheric state was the horizontally uniform model atmosphere used to calculate the weighting function. The perturbed state was constructed by adding a 1 K amplitude ($\tilde{T}$) GW in the x-z plane whose temperature perturbation, T', had the functional form:

$$T' = \tilde{T} \mathrm{e}^{i(kx+mz)} \tag{1}$$

,

where k and m are the horizontal and vertical wavenumbers. **This equation is a simplification of Eq. 1 of Heavens et al. (2020) that accounts for waves being observed much faster than their intrinsic period, so that they can be regarded as being observed at a fixed instant of time equivalent to t=0.**

By varying the wavenumbers, the visibility then was calculated for each model atmosphere and channel by: (1) convolving the weighting functions for each detector with the model atmosphere

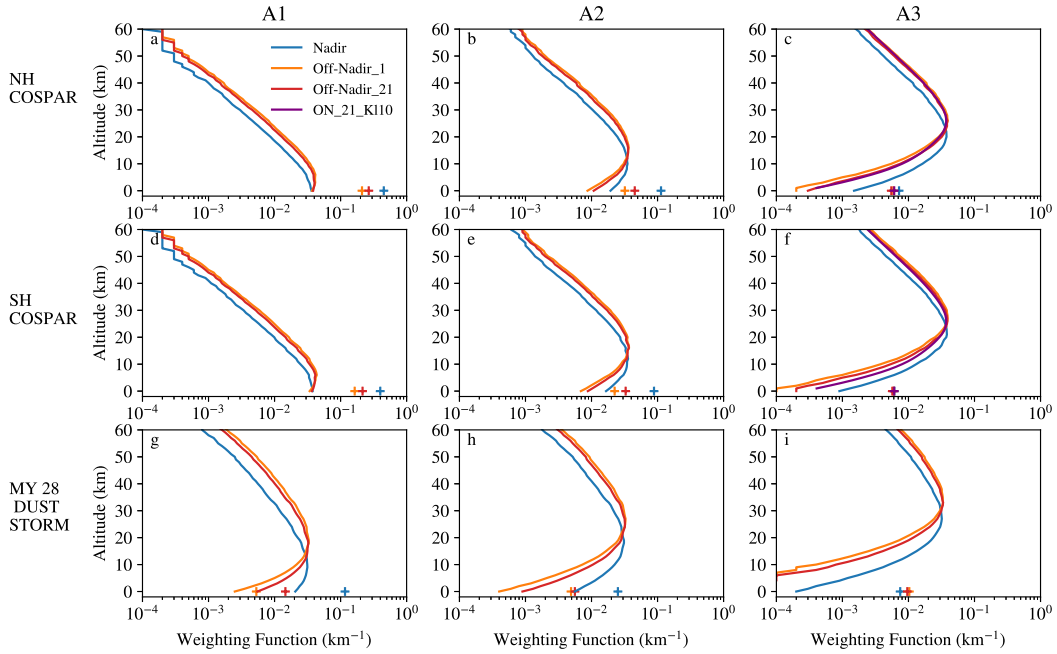

Figure 2. Comparison of the vertical weighting functions for the MRO-MCS A1–A3 channels and off-nadir geometry for detectors 1 and 21 for the three input atmospheres, as labeled. The estimated surface contributions are marked with crosses at 0 km altitude in each panel. The weighting functions have been plotted over a more limited vertical range than calculated to emphasize the altitudes at which they peak. ON_21_Kl10 refers to the off-nadir weighting function for detector 21 of the A3 channel (assuming an observation of 9° below the limb) calculated by Kleinböhl et al. (2010), which was obtained from A. Kleinböhl.

.

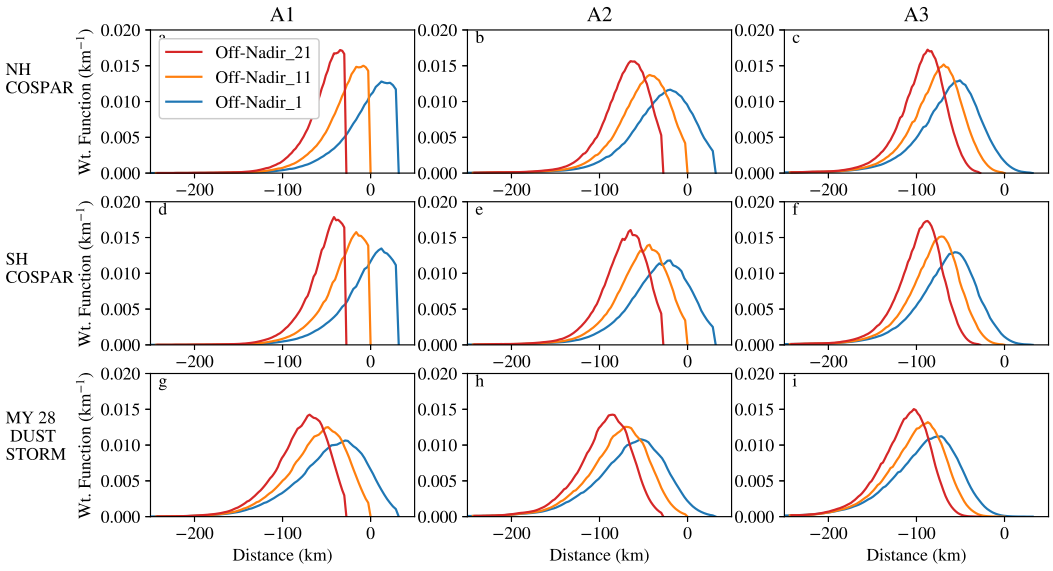

Figure 3. Comparison of the horizontal weighting functions for the MRO-MCS A1–A3 channels and off-nadir geometry for detectors 1, 11, and 21 for the three input atmospheres, as labeled. The weighting functions have been plotted so that they are relative to the intersection point of the optical path of detector 11 (the central detector) with the surface.

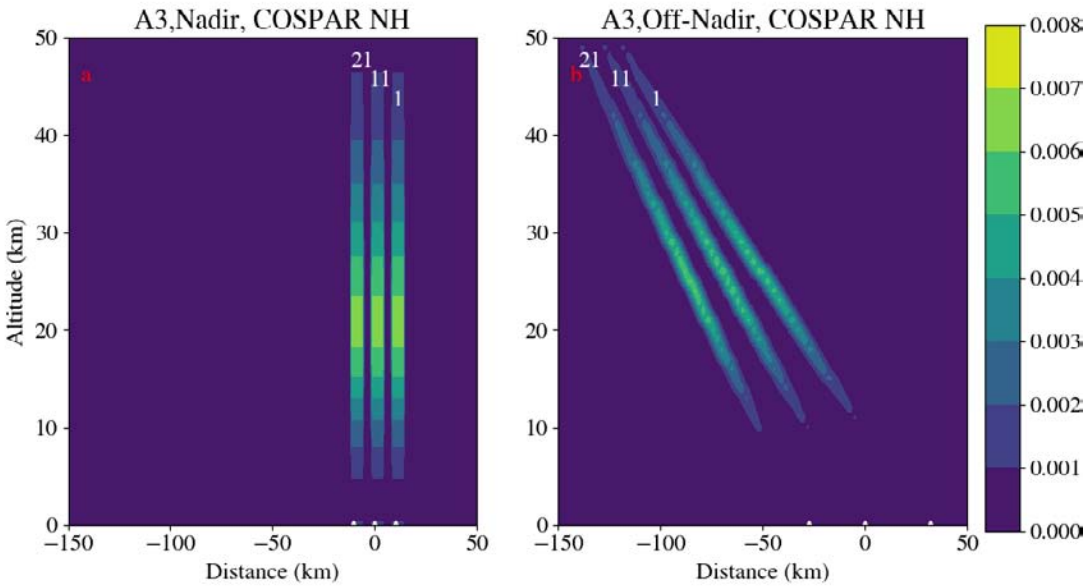

Figure 4. Two-dimensional weighting functions (km^{-2}) for the MRO-MCS A3 channel and off-nadir geometry for detectors **21, 11, and 1** for the COSPAR Northern Hemisphere atmosphere, as labeled. The weighting functions have been plotted so that they are relative to the intersection point of the optical path of detector 11 **(the central detector of the line of detectors in a channel)** with the surface. Intersection points with the surface for each of the plotted detectors is indicated with white markers at 0 km altitude.

to calculate the simulated brightness temperature; (2) then calculating the brightness temperature variance measured across the simulated detector array according to the protocol outlined by Heavens et al. (2020); (3) normalizing this variance by 0.5 K^2, the variance of a sine or cosine wave with an amplitude of 1 K; and (4) then converting to a percentage.

2.1.3. *Results of the visibility analysis*

Although calculated more rigorously, the results of the visibility analyses are consistent with those of Heavens et al. (2020). Nadir views in A2 and A3 are most sensitive to horizontal wavelengths, λ_h, of 10–30 km and vertical wavelengths, $\lambda_z > 50$ km (Figs. 5b–c, e–f, h–i). Substantial visibility for A1 under clear conditions extends to the smallest vertical wavelengths sampled but is strongest at λ_h of 10–30 km and $\lambda_z > 50$ km (Figs. 5a,d). Under dusty conditions, A1 visibility is similar to A2 and A3 visibility under all circumstances (Figs. 5g).

Following Heavens et al. (2020), visibility plots like this can be interpreted to constrain the intrinsic period of the observed waves by adopting the relation that for λ_z sufficiently smaller than 120 km in Mars's atmosphere, the intrinsic frequency, $\hat{\Omega_{GW}}$ (wind-relative frequency of a GW), is:

$$\hat{\Omega_{GW}} = \frac{N}{\sqrt{1 + \left(\frac{\lambda_h}{\lambda_z}\right)^2}} \tag{2}$$

(Fritts & Alexander 2003),

where N is the Brunt-Väisälä frequency (0.008 s^{-1}: Imamura et al. (2007); Ando et al. (2012)).

So the A2 and A3 channels in nadir geometry generally observe GW with periods $< 20\%$ greater than N^{-1}, that is, a few minutes, while A1 has some sensitivity to periods of up to an hour ($30N^{-1}$), though generally much shorter.

The calculated off-nadir visibilities also have forms very similar to those presented in Heavens et al. (2020) (Figs. 6a–i). There is some sensitivity starting at λ_h of 10 km and λ_z of 5 km and continuing along a parabolic slope to λ_h of 80 km and λ_z of 30 km, where there is weak visibility at larger vertical wavelengths, particularly in A1 and A2 . The magnitude of visibility generally peaks near λ_h of 30–40 km and λ_z of 10–20 km. The periods corresponding to this range are $\approx (10N^{-1})$ or 20 minutes.

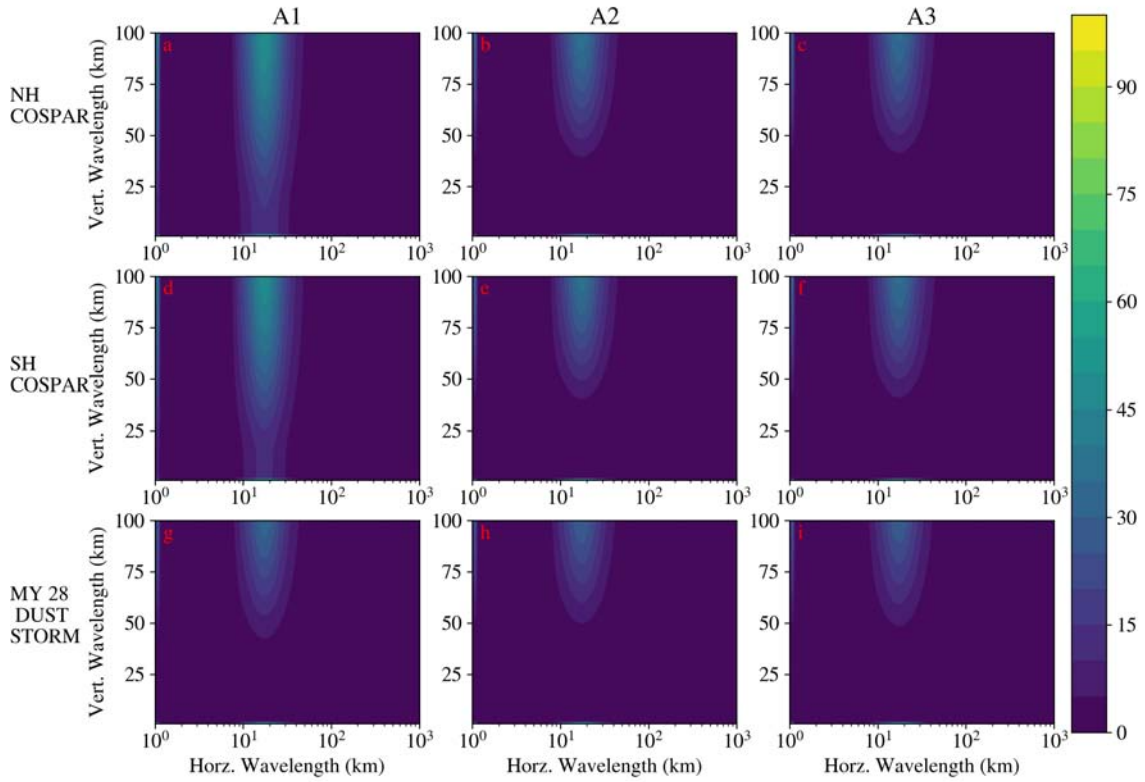

Figure 5. Comparison of the estimated visibility to GW (%) with the given horizontal and vertical wavelengths of the MRO-MCS A1–A3 channels and nadir geometry for the three input atmospheres, as labeled.

A1 under clear atmospheric conditions can have peak visibility > 100% and substantial visibility at all wavelengths (Figs. 6a,d). This is a consequence of its weighting function sloping and peaking near the surface, which introduces detector to detector oscillations connected to the increase or decrease of temperature with altitude as opposed to the oscillations introduced by the gravity wave perturbations. This effect vanishes if the temperature profile is vertically uniform and can be strengthened or weakened by adjusting the lapse rate near the surface in the visibility simulations. Thus, A1 could be sensitive not just to GW variability but also to the vertical lapse rate in the lowest 15–20 km of the atmosphere. Peak visibility is ≈ 75% in A2 and ≈ 60% in A3 in clear conditions.

3. METHODS

3.1. *Analysis of the MRO-MCS Level 1B dataset*

The MRO-MCS Level 1B dataset MCS (cited 2020) was analyzed according to the procedure outlined in (Heavens et al. 2020) with a few modifications.

The data analyzed was restricted to all forward, in-track (180° azimuth), on-planet (scene altitude of zero) observations in the A1, A2, A3, and B1 channels between the beginning of the mission and $L_s = 128.84°$ of MY 35 (the end of 2019). Nadir observations were defined as on-planet observations with elevations between 177° and 183°. Off-nadir observations were defined as on-planet observations with elevations between 117° and 123°. In addition, observations were only included if they had "Gqual" and "Moving" flags equal to zero and had a top detector (detector 1) radiance greater than zero.

To exclude the calibration-related artifacts described by Heavens et al. (2020), the observations were filtered by including on-planet radiance measurements only if the detector 1 radiances in the A1, A2, A3, and B1 channels in the preceding space view had a magnitude less than 0.4 mW m^{-2} $(cm^{-1})^{-1}$ sr^{-1} and the sum of the radiances over all detectors in each of the A1, A2, A3 and B1 channels in the preceding space view had a magnitude less than 1.52 mW

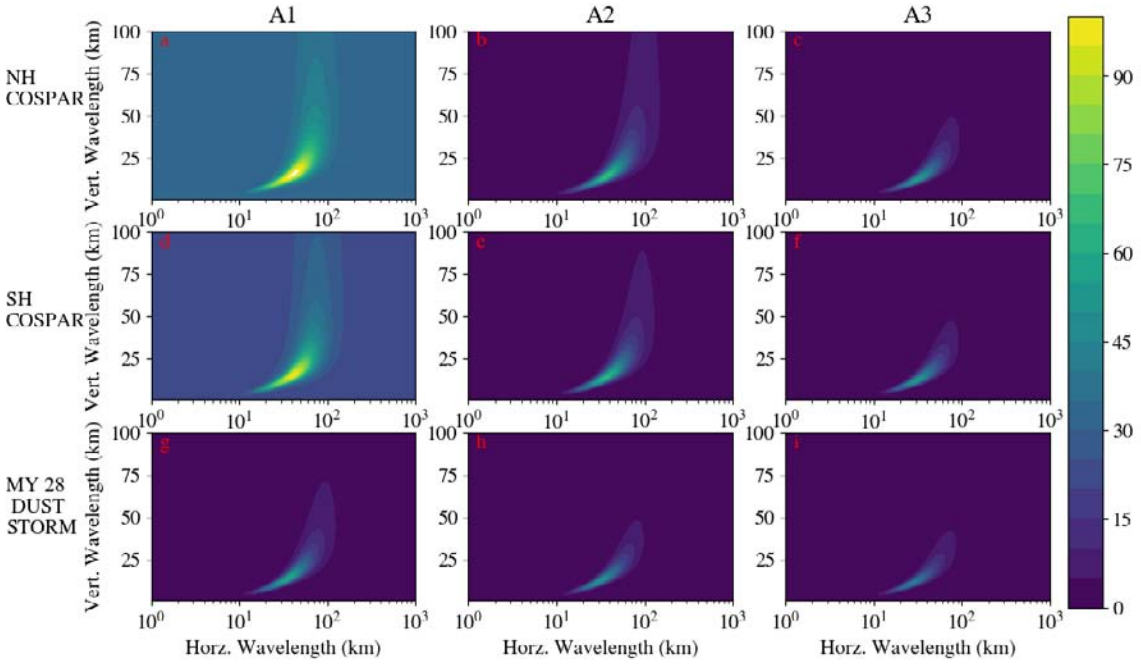

Figure 6. Comparison of the estimated visibility to GW (%) with the given horizontal and vertical wavelengths of the MRO-MCS A1–A3 channels and off-nadir geometry for the three input atmospheres, as labeled.

m^{-2} $(cm^{-1})^{-1}$ sr^{-1}, and the prior and subsequent limb views had detector 1 radiances in the A1, A2, A3, and B1 channels greater than -0.4 mW m^{-2} $(cm^{-1})^{-1}$ sr^{-1}.

In Heavens et al. (2020), these criteria only were applied to A3. Heavens et al. (2020) notes that the first and third criteria are based on the noise threshold of the instrument. The second is presumably empirical but likewise should scale with instrument noise. These criteria seemed reasonable to apply to all channels, because the estimated radiance noise in A1 (the noisiest channel among the 4 studied) is only 33% greater than that of A3 (Kleinböhl et al. 2009). An additional consequence of this is that the uncertainties in GW variance diagnoses for the channels other than A3 will be within a factor of 2 of those in A3 for equivalent temperatures.

We identified additional calibration-related artifacts associated with breaks in the normal observation pattern of on-planet views that lasted an orbit or more. We therefore excluded any pair of on-planet views that took place more than 300 s after the previous set of on-planet views. This filter reduced the number of diagnoses by $< 0.1\%$ from the unfiltered condition.

Then, Ω_{GW} (the GW variance in an observation), ϵ_{GW} (the 1σ uncertainty in GW variance in an observation), $\hat{\Omega_{GW}}$ (the GW variance in an observation normalized by the mean of the squared temperature in each measurement within the observation), $\epsilon_{\hat{GW}}$ (the 1 σ uncertainty in the normalized variance), and relevant time/location/elevation/roughness information were calculated for each individual observation. The variance and error calculations were made for each of the A channels in the same way as in Heavens et al. (2020), just using the appropriate band central wavenumber and radiance error in Kleinböhl et al. (2009) for each individual channel studied. However, the central wavenumber for B1 was varied by detector to account for the more variable intra-channel spectral response of B detectors (Kleinböhl et al. 2011).

The position of each detector in each channel relative to the position of the scene observed by the center of the detector array was computed by re-projecting the MCS detector array in Cartesian space along the orbital track of the spacecraft, taking account of crossing the anti-prime meridian. The mean latitude and longitude of the observation then were estimated to be the position of detector 11, **the central detector of each channel**. The mean elevation relative to the areoid was calculated by interpolating the positions of each detector on the 16 point per degree MOLA elevation map available from the NASA Planetary Data System (PDS) (Smith et al. 2003) and taking the mean of the elevations for all detectors. The maximum elevation in all detectors was also recorded to enable identification of

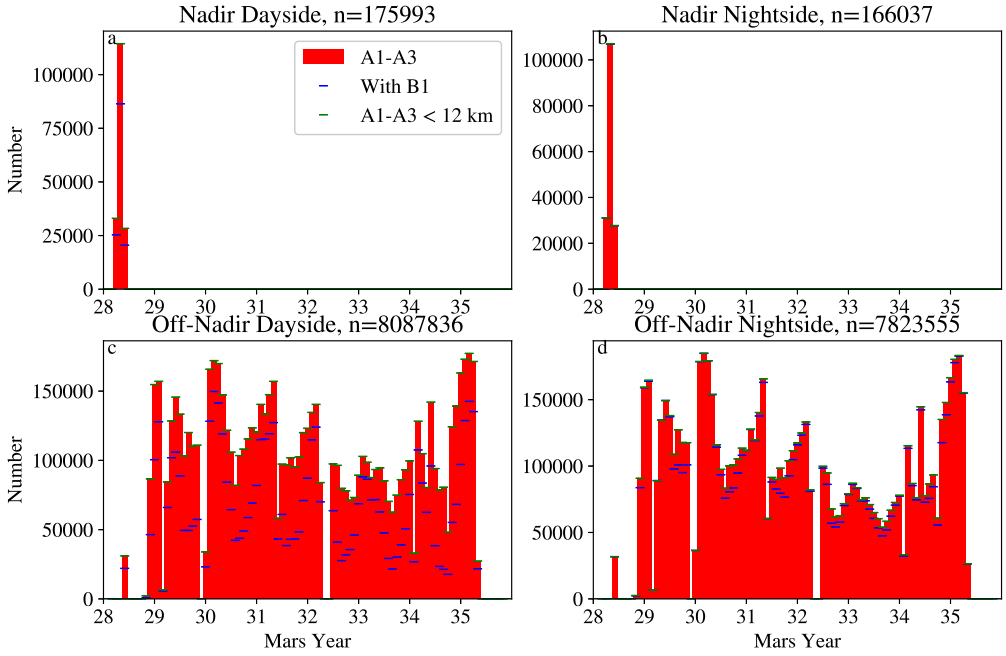

Figure 7. The number of analyzed nadir and off-nadir observations, binned by 30° of L_s, and nightside vs. dayside, as labeled. The titles report the total number of observations analyzed for the A1–A3 survey. The red bars indicate the total amount of observations for the A1–A3 survey; the blue horizontal lines indicate the number of observations available for the survey with B1 included; the green horizontal lines indicate the number of observations for the A1–A3 survey where the maximum surface elevation for any detector in A3 is less than 12 km (the numbers in the other channels are similar).

observations with potentially significant surface contributions. The roughness at the scale of the observation in then calculated from the variance of the elevations corresponding to the detectors. Nightside observations were distinguished from dayside observations by determining from the scene location information whether the spacecraft was ascending in latitude on dayside or descending in latitude on the nightside.

One consequence of applying the space view-based filter to A1, A2, A3, and B1 simultaneously was to reduce the density of coverage substantially. This can be illustrated by comparing the number of total off-nadir diagnoses between our survey and that of Heavens et al. (2020) over the period studied by Heavens et al. (2020) (MY 28, L_s =111.2823°–MY 34, L_s = 232.643°). In Heavens et al. (2020), there were 6,661,256 total off-nadir diagnoses on the nightside compared to 6,314,719 in our survey (5.2% less); on the dayside, there were 6,994,855 total diagnoses by Heavens et al. (2020) but only 4,573,202 diagnoses in our survey (34.6% less). Therefore, the survey was repeated with A1, A2, A3 alone, to eliminate the need to include B1 in the filter. There were 6,646,544 nightside diagnoses over the period considered by Heavens et al. (2020) (0.2% less), while there were 6,963,000 dayside diagnoses over the same period (0.5% less). Therefore, the A1–A3 channel dataset is nearly identically dense in coverage to the A3 dataset of Heavens et al. (2020), with typically 50,000–170,000 dayside or nightside observations in a bin of 30° of L_s (Fig. 7a–d). Because the focus of this study is variability in atmospheric temperature due to atmospheric waves rather than surface temperature, we therefore restricted the remainder of our analysis to the A1–A3 channel dataset. While a recent analysis by Hinson & Wilson (2021) suggests B1 may be sensitive to atmospheric variability in the lowermost atmosphere under some circumstances in the extratropics, this may not be necessarily globally applicable.

In map view, the Ω_{GW} and ϵ_{GW} data was binned by dayside/nightside and by 30° of L_s and averaged at 1°× 1°, 2°× 2°, and 5°× 5° resolution. $\hat{\Omega_{GW}}$ and $\hat{\epsilon_{GW}}$ were likewise calculated and averaged in the same way. Averages were made of the available data from individual Mars Years as well as of all of the data in MY 29–33 and 35, to better infer differences between years with (that is, MY 28 and MY 34) and without global dust storm activity. In order to better study intraseasonal variability, the Ω_{GW} and ϵ_{GW} data was binned by dayside/nightside and by 9° of L_s and

averaged at 5°× 5°. Following Heavens et al. (2020), a momentum flux metric also was calculated from the off-nadir observations:

$$\tilde{F_{ph}} = \frac{1}{(\bar{T^2})^{1/2}} \hat{\Omega_{GW}} \tag{3}$$

where $(\bar{T^2})^{1/2}$ is the square root of the mean squared temperature.

To characterize the intermittency of GW sources, we followed Heavens et al. (2020) in using the intermittency metric of Hertzog et al. (2008); Wright et al. (2013): the percentage of total momentum flux in the top 10% of momentum flux diagnoses relative to the integrated momentum flux in the distribution. To minimize spurious extrapolations, this intermittency metric only was calculated when at least 10 diagnoses of Ω_{GW} are available in the given spatial/seasonal/time of day bin. Therefore, there is only enough data from non-dust storm years to generate visually acceptable intermittency maps with minimal unfilled bins at a resolution of 30° of L_s and a spatial resolution of 2°× 2°.

Zonal averaging was performed on a grid binned by MY, dayside/nightside, 2° in L_s, 2° in latitude, and 10 ° in longitude. MRO makes approximately 50 orbits per 2° of L_s, and MCS makes a pair of on-planet observations approximately every 2° in latitude, so this averaging resolution enables there to be at least one data point per longitude bin when there are 50,000 diagnoses per 30° of L_s at a given time of day. Averaging is done by longitude bin at a given latitude and then the average of all longitude bins is made. Global averaging was performed by taking the average of the zonal average data weighted by cosine of the central latitude of each latitude bin.

While averages were calculated with and without observations where the maximum elevation was > 12 km, inspection of Heavens et al. (2020) and the analysis in **Appendix** A suggests only the results with high elevation surfaces excluded are worth presenting. Likewise, Heavens et al. (2020) demonstrates that the behavior of the non-normalized quantities (e.g., Ω_{GW} and ϵ_{GW}) is generally similar to the normalized quantities, only the normalized quantities will be presented. These normalized quantities can be related to GW specific energy density and the vertical flux of horizontal momentum (Ern et al. 2004; Heavens et al. 2020).

3.2. *Roughness information*

Creasey et al. (2006) observed that orographic GW parameterizations in global climate models typically related the gravity wave flux to the surface stress, which is a function of atmospheric density (ρ), N, the magnitude of low level wind, and the topographic variance (surface roughness). Heavens et al. (2010) followed Creasey et al. (2006) in trying to estimate surface stress based on information from the Mars Climate Database (Millour et al. 2015) and the average of the surface roughness estimates in the MRO-MCS radiance observations. This analysis suggested that surface stress varied minimally seasonally, implying that the surface stress is dominantly a function of the surface roughness. Therefore, the surface roughness distribution should be a good hypothesis for the distribution of orographic GW activity.

The surface roughness therefore was estimated by averaging the topographic variance in all off-nadir observations in the A2 channel at surface elevations < 12 km at a spatial resolution of 1°× 1°, 2°× 2°, and 5°× 5°. The A2 channel is directly between A1 and A3 in the MRO-MCS detector array (McCleese et al. 2007). Topographic maps at the same resolutions were generated by averaging similarly filtered elevation data. **A roughness map stretched to emphasize major roughness features has been included as Fig. 8 and can be used as a geographic reference throughout the remainder of the paper.**

4. RESULTS

4.1. *A changing global distribution of GW activity with altitude*

4.1.1. *Nadir observations*

Nadir observations were limited to a brief period early in the MRO-MCS mission. GW activity observed from the nadir during this time was generally stronger lower in the atmosphere and stronger on the dayside than the nightside (Figs. 9a–f). Heavens et al. (2020) argued that GW activity in the dayside tropics in A3 observations was stronger over high elevation areas than low elevation areas. However, the A1 and A2 nadir observations (particularly A2 at night) show substantial GW activity associated with Valles Marineris (15° S–0° N, 100–45° W), which reaches elevations as low as -4500 m (Figs. 9a–b, d–e). Another notable feature in A1 and A2 dayside observations (Figs. 9a–b) is a planet-encircling band of substantial GW activity at 50° S, which is absent in A3.

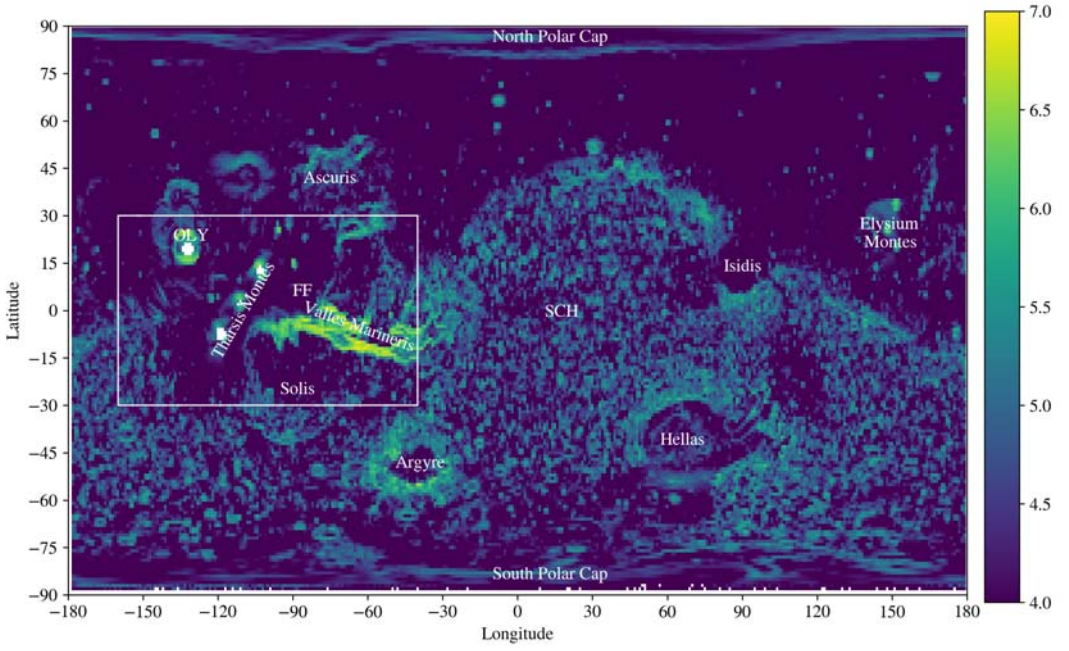

Figure 8. Log_{10} of the estimated surface roughness (m^2) labeled with important geographic features mentioned the text. The scale is saturated at 4 and 7 log units to emphasize the roughest features on Mars. Abbreviations OLY (Olympus Mons), FF (Fortuna Fossae), and SCH (Schiaparelli Crater) are used to label smaller-scale features. The rectangular box marks a region of interest plotted in panels within Figs. 14–16.

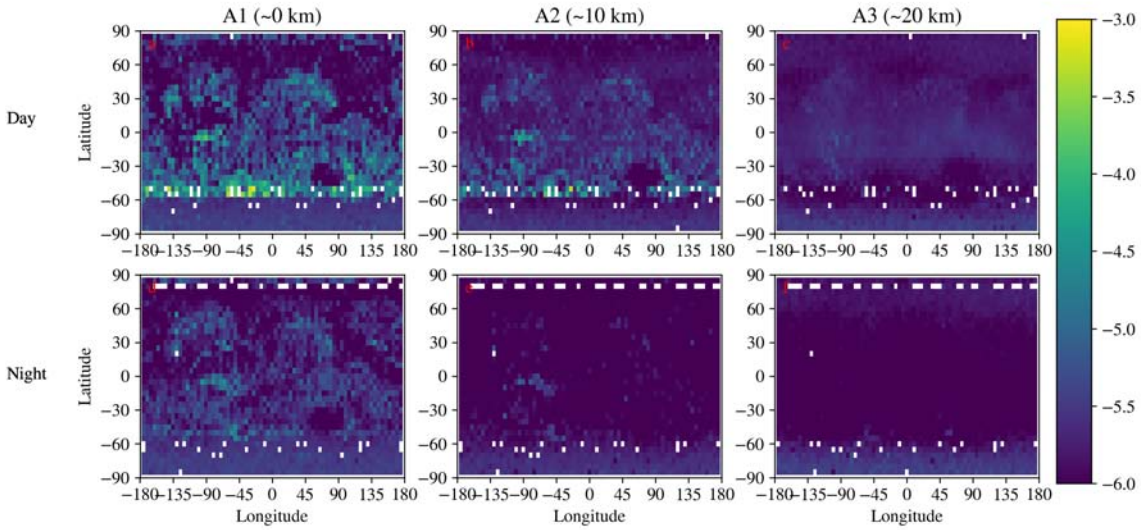

Figure 9. Mean spatial distribution of GW activity viewed from nadir observations during L_s=120°–150° of MY 28 averaged at 5° resolution expressed as $log_{10}\hat{\Omega_{GW}}$ (K^2 K^{-2}) for the channel and time of day labeled. White space indicates that no data is available in the averaging bin. The lower end of the plotting colorscale is saturated at 10^{-6} K^2 K^{-2}, the approximate uncertainty in the planet's coldest areas (the southern polar cap).

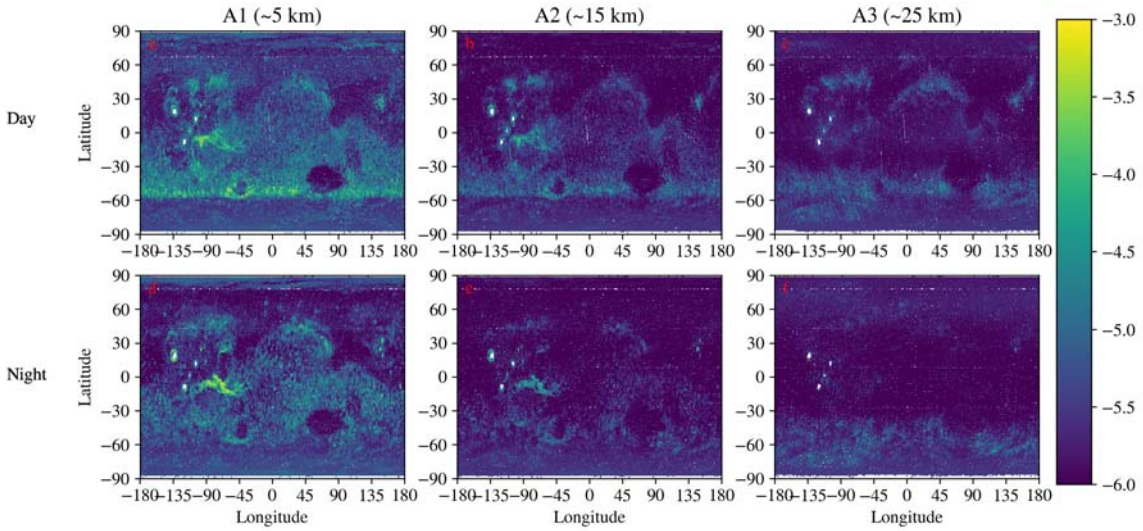

Figure 10. Mean spatial distribution of GW activity viewed from off-nadir observations during L_s=120°-150° of MY 29–33,35 averaged at 1° resolution expressed as $log_{10}\hat{\Omega_{GW}}$ (K^2 K^{-2}) for the channel and time of day labeled. White space indicates that no data is available in the averaging bin. The lower end of the plotting colorscale is saturated at 10^{-6} K^2 K^{-2}, about an order of magnitude larger than the approximate uncertainty in the planet's coldest areas (the southern polar cap).

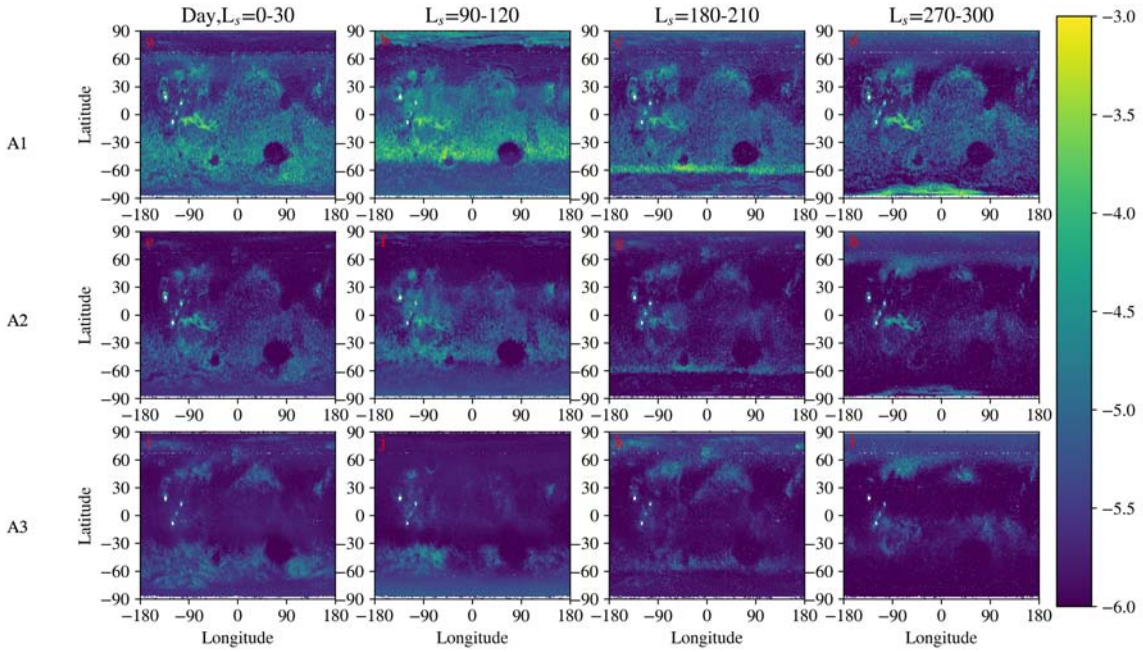

Figure 11. Mean spatial distribution of GW activity viewed from dayside off-nadir observations during MY 29–33,35 averaged at 1° resolution expressed as $log_{10}\hat{\Omega_{GW}}$ (K^2 K^{-2}) for the season labeled. White space indicates that no data is available in the averaging bin. The lower end of the plotting colorscale is saturated at 10^{-6} K^2 K^{-2}, about an order of magnitude larger than the approximate uncertainty in the planet's coldest areas (the winter polar cap).

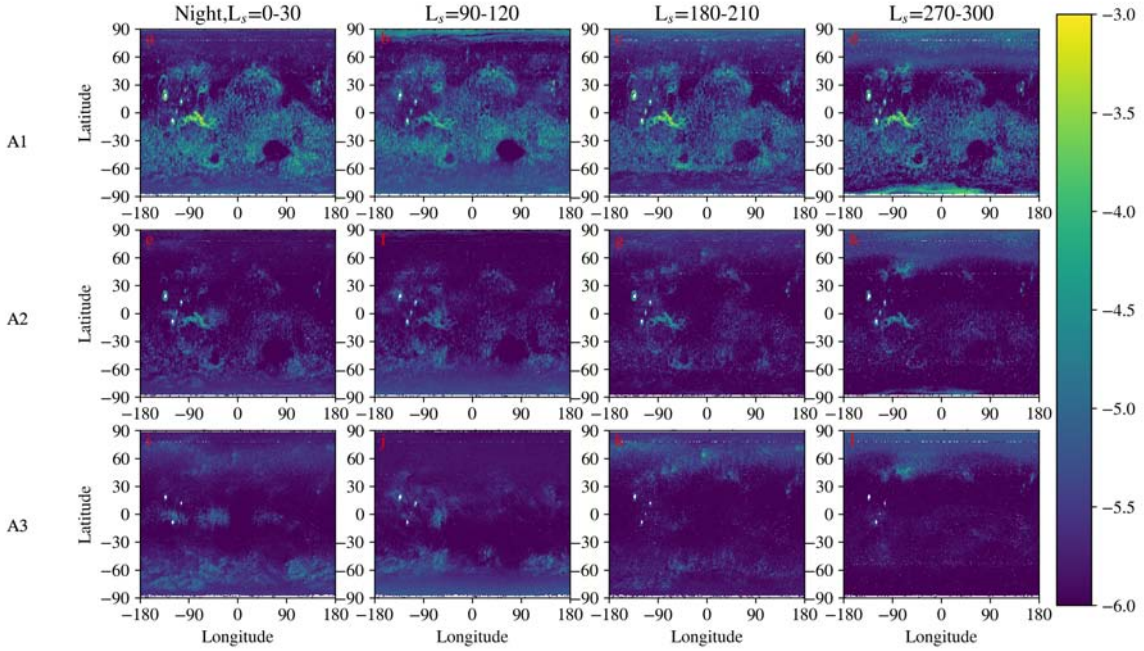

Figure 12. Mean spatial distribution of GW activity viewed from nightside off-nadir observations during MY 29–33,35 averaged at 1° resolution expressed as $log_{10}\hat{\Omega_{GW}}$ (K^2 K^{-2}) for the season labeled. White space indicates that no data is available in the averaging bin. The lower end of the plotting colorscale is saturated at 10^{-6} K^2 K^{-2}, about an order of magnitude larger than the approximate uncertainty in the planet's coldest areas (the winter polar cap).

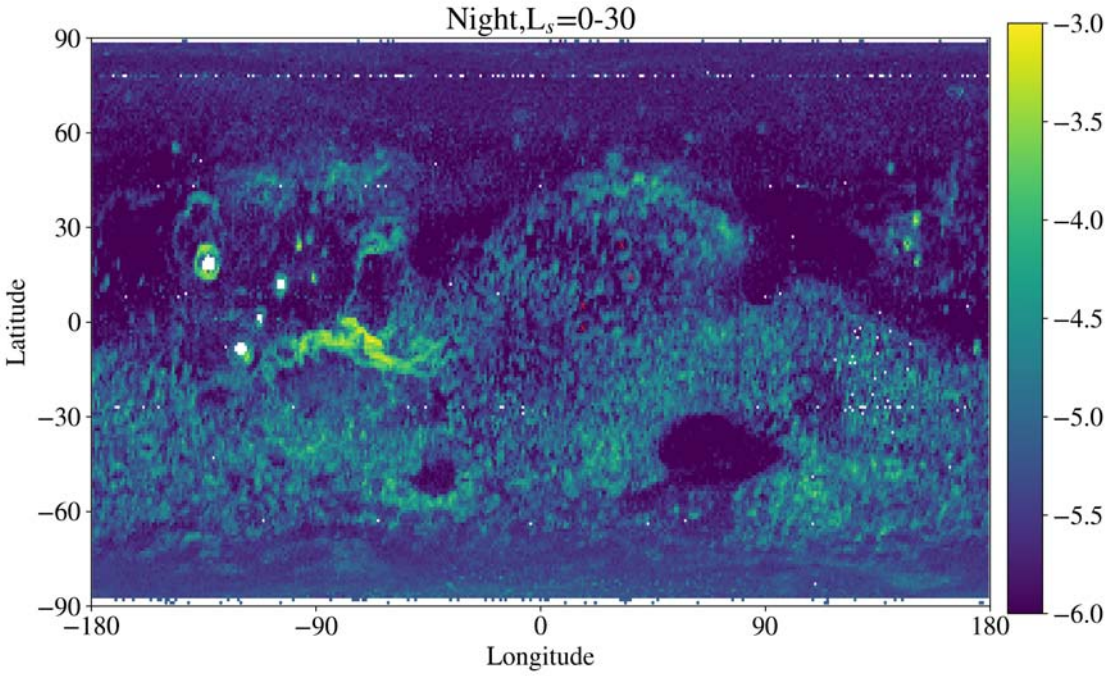

Figure 13. Identical to Fig. 12a, except that the center of a few example circular structures in GW activity near 15° N, 30°E have been marked with red xs.

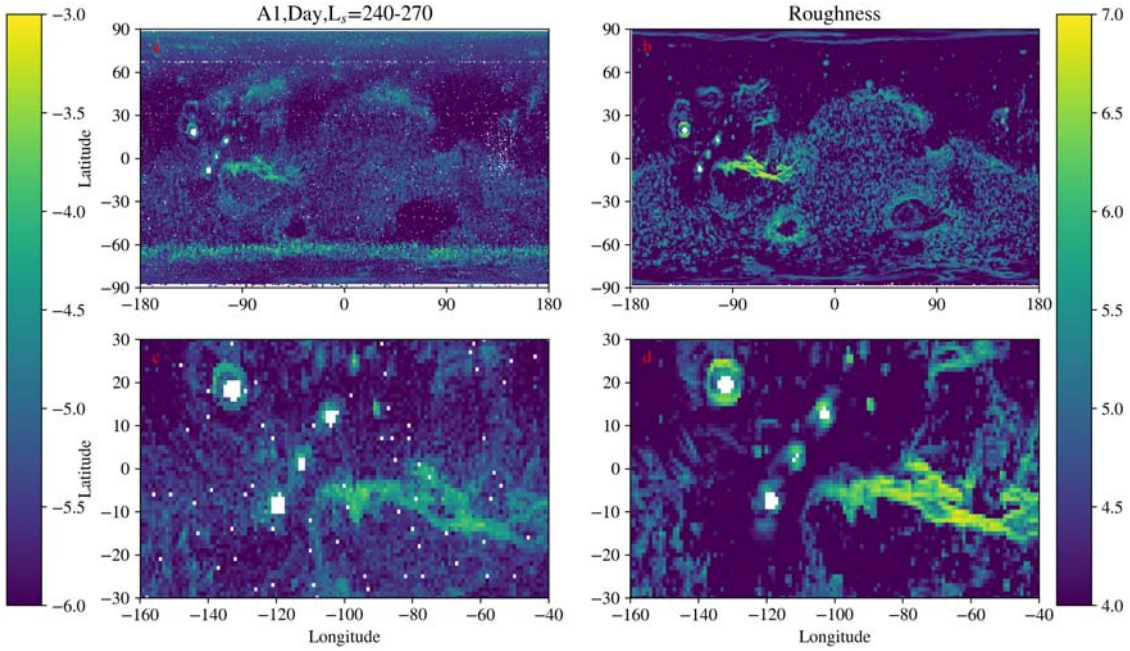

Figure 14. Spatial distribution of GW activity compared with surface roughness: (a) Mean spatial distribution of GW activity viewed from dayside off-nadir observations in A1 during L_s of 240°–270° of MY 29–33,35 averaged at 1° resolution expressed as $\log_{10}\hat{\Omega_{GW}}$ (K^2 K^{-2}). White space indicates that no data is available in the averaging bin. The lower end of the plotting colorscale is saturated at 10^{-6} K^2 K^{-2}, about an order of magnitude larger than the approximate uncertainty in the planet's coldest areas (the winter polar cap); (b) Log_{10} of mean roughness (m^2) at the baseline of off-nadir observations averaged at 1° resolution; (c) identical to (a) but focused on 30° S–30° N, 160°–40° W; (d) identical to (b) but focused on 30° S–30° N, 160–40° W.

4.1.2. *Off-nadir observations*

As in the nadir, GW activity viewed in the off-nadir is generally stronger lower in the atmosphere**.** Valles Marineris is a prominent area of GW activity in A1 and A2 (but not in A3), and there is a band in GW activity on the dayside at 50° S that perhaps spreads in width with altitude (Figs. 10a–f). The variability in A1 has significant structure near the resolution of averaging, which has disappeared in most tropical areas in A3.

The presence of a narrow band of substantial GW activity in the southern extratropics **(near 50°)** on the dayside in A1 and A2 is only apparent in two of the periods presented and in A3 during only one (Figs. 11b–c,f–g,k). But GW activity in Valles Marineris and structure in GW activity near the resolution of averaging are apparent in A1 and A2 throughout the year (Figs. 11a–h;12a–h).

This high resolution structure maps closely onto large craters. The most prominent craters with such structure in all channels are the Argyre (50° S, 60° W) and Hellas (40° S, 80° E) Basins in the southern extratropics. But smaller circular features can be seen in A1. One example is centered near 5° S, 15° E, corresponding to the 458 km (≈ 8°) diameter crater, Schiaparelli (Figs. 12a,13). Higher activity is observed near the raised edge of this crater than its center, resulting in a circular feature. In other words, the distribution of GW activity in A1 and A2 appears to be shaped by variability in surface roughness.

4.1.3. *Correlation with surface roughness*

Direct comparison of GW activity in A1 with surface roughness suggests a close relationship. Fine structure near the resolution of the map is clearer in the surface roughness map (Fig. 14b) than in the $\hat{\Omega_{GW}}$ map for A1 (Fig. 14a) and accentuates Schiaparelli and other similar-sized craters. The surface roughness map also shows that Valles Marineris is the roughest area of Mars. In the elevated volcanic province of Tharsis and Valles Marineris, roughness features at a variety of scales are areas of high GW activity. Valles Marineris is prominent but so are Olympus Mons

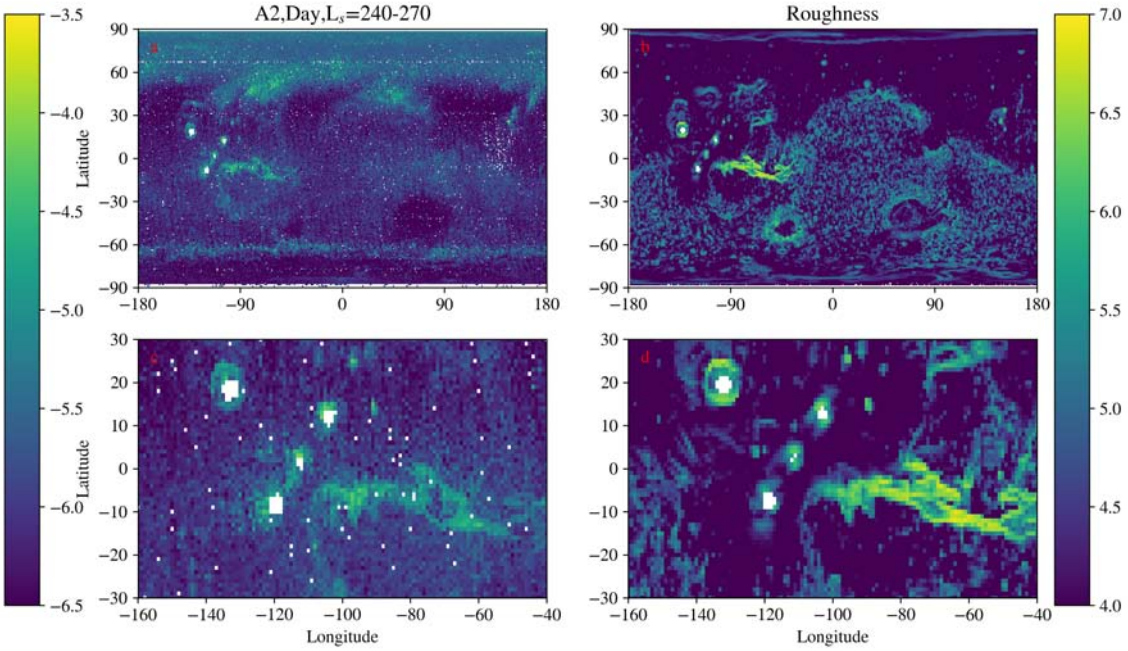

Figure 15. Spatial distribution of GW activity compared with surface roughness: (a) Mean spatial distribution of GW activity viewed from dayside off-nadir observations in A2 during L_s of 240°–270° of MY 29–33,35 averaged at 1° resolution expressed as $\log_{10}\hat{\Omega_{GW}}$ (K^2 K^{-2}). White space indicates that no data is available in the averaging bin. The lower end of the plotting colorscale is saturated at 10^{-6} K^2 K^{-2}, about an order of magnitude larger than the approximate uncertainty in the planet's coldest areas (the winter polar cap); (b) Log_{10} of mean roughness (m^2) at the baseline of off-nadir observations averaged at 1° resolution; (c) identical to (a) but focused on 30° S-30° N, 160°–40° W; (d) identical to (b) but focused on 30° S–30° N, 160–40° W.

Table 1. Correlation **(product-moment)** (r) of elevation (m) or $\log_{10}$ of roughness (m^2) with $\log_{10}$ of Ω_{GW} (K^2) for all observations in the labeled viewing geometry in 30° S-30° N during L_s=120°-150° of all sampled MY. n is the number of observations used. Observations where the maximum elevation was greater than 12 km have been excluded.

Nadir	A1		A2		A3	
	Elevation	Roughness	Elevation	Roughness	Elevation	Roughness
Day, r	0.12	0.60	0.13	0.38	0.28	0.10
n	45,354		45,351		45,351	
Night, r	0.15	0.43	0.14	0.34	-0.47	-0.05
n	45,390		45,389		45,379	
Off-nadir	A1		A2		A3	
	Elevation	Roughness	Elevation	Roughness	Elevation	Roughness
Day, r	0.32	0.40	0.35	0.29	0.20	0.05
n	214,588		214,595		214,635	
Night, r	0.13	0.49	0.15	0.32	-0.05	0.00
n	210,887		210,897		210,912	

and the Tharsis Montes (the circular features with white space in the middle, where observations over high elevation data have been excluded) (Figs. 14c-d). Activity is also high around some roughness features of both positive and negative topography near 20° N, 90° W. These include Ceraunius and Uranius Tholi (near 25° N, 100° W), Uranius Mons (near 25° N, 95° W), Tharsis Tholus (near 15° N, 90° W), and Fesenkov Crater (near 20° N, 85° W). Further east, GW activity seems to weakly illuminate the area around Sacra Mensa (near 25° N, 65° W). There is one feature

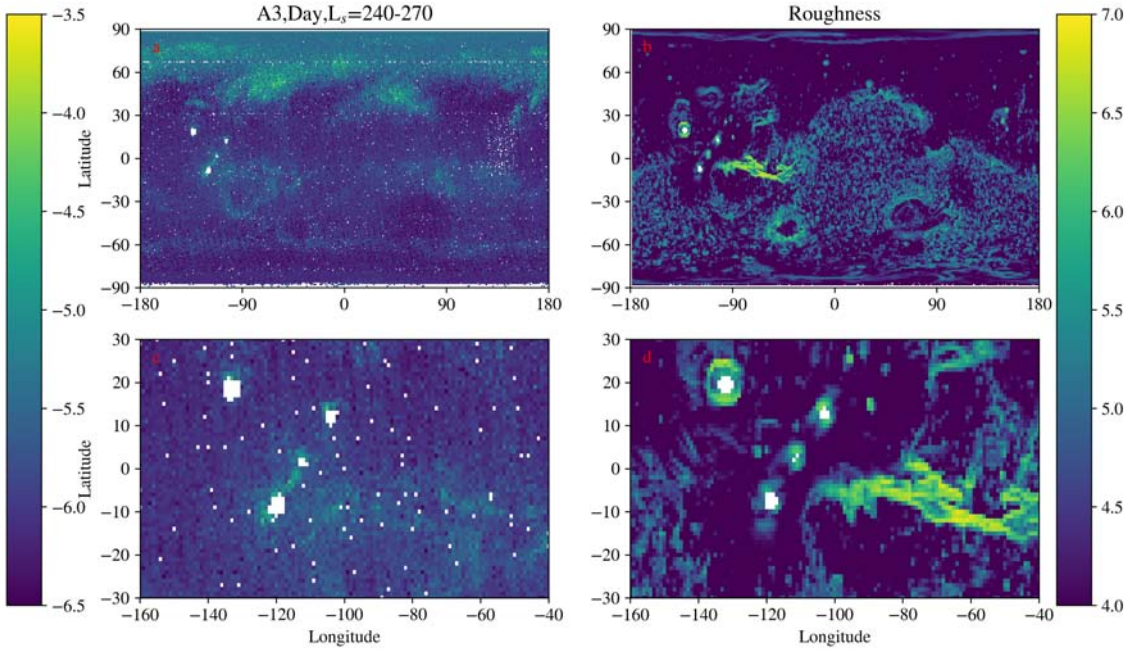

Figure 16. Spatial distribution of GW activity compared with surface roughness: (a) Mean spatial distribution of GW activity viewed from dayside off-nadir observations in A3 during L_s of 240°–270° of MY 29–33,35 averaged at 1° resolution expressed as $\log_{10}\hat{\Omega_{GW}}$ (K^2 K^{-2}). White space indicates that no data is available in the averaging bin. The lower end of the plotting colorscale is saturated at 10^{-6} K^2 K^{-2}, about an order of magnitude larger than the approximate uncertainty in the planet's coldest areas (the winter polar cap); (b) Log_{10} of mean roughness (m^2) at the baseline of off-nadir observations averaged at 1° resolution; (c) identical to (a) but focused on 30° S–30° N, 160°–40° W; (d) identical to (b) but focused on 30° S–30° N, 160–40° W.

in the A1 GW activity map that does not appear to have anything to do with roughness, the band of activity near 65° S (Fig. 14a), but otherwise roughness appears to be explanatory.

In A2, the fine structure mostly disappears (Fig. 15a) but Valles Marineris, Olympus Mons and the Tharsis Montes, and some of the small topographic features (generally the positive ones) are marked by GW activity (Fig. 15c). In parallel, rough regions in the northern extratropics that were less prominent in A1, such as the areas around Ascuris Planum and Mareotis Fossae (near 45°N, 80°W) and the dichotomy boundary northwest of the Isidis Basin (15°N, 90°E) are more prominent in A2 (Fig. 15a). In A3, GW activity associated with the low altitude areas of Valles Marineris disappears, but Olympus Mons and the Tharsis Montes are still apparent (Fig. 16c). Argyre and Hellas are visible, as is the roughness associated with the margins of Valles Marineris and the southern margin of Solis Planum (near 40° S, 90° W) (Fig. 16a). The areas near Ascuris Planum and Mareotis Fossae and to the northwest of Isidis are the strongest areas of GW activity in A3, though they appear broader in area than the roughness features and are joined by other features in the northern extratropics that do not have obvious association with roughness **such as the area centered near 75° N, 120° W** (Fig. 16a–b). The band in the southern extratropics remains apparent in A3 but smaller in magnitude than the GW activity in the northern extratropics.

At 1° resolution, surface roughness moderately correlates with GW activity in A1 (Figs. 17a,d). This correlation is weaker near southern summer solstice **(L_s=270°, the boundary between Mars months 9 and 10)** and at night but is generally stronger and less variable with season around the Tharsis Montes and Valles Marineris. Correlation between roughness and GW activity in A2 is weaker than in A1 (Figs. 17a–b,d–e); roughness and GW activity do not appear to be correlated in A3 (Figs. 17c,f).

Heavens et al. (2020) demonstrated some correlation between elevation and tropical GW activity in A3 dayside nadir observations and moderate anti-correlation on the nightside. This relationship was less apparent in off-nadir observations. Adding A1 and A2 channels and roughness to a similar correlation analysis suggests that surface

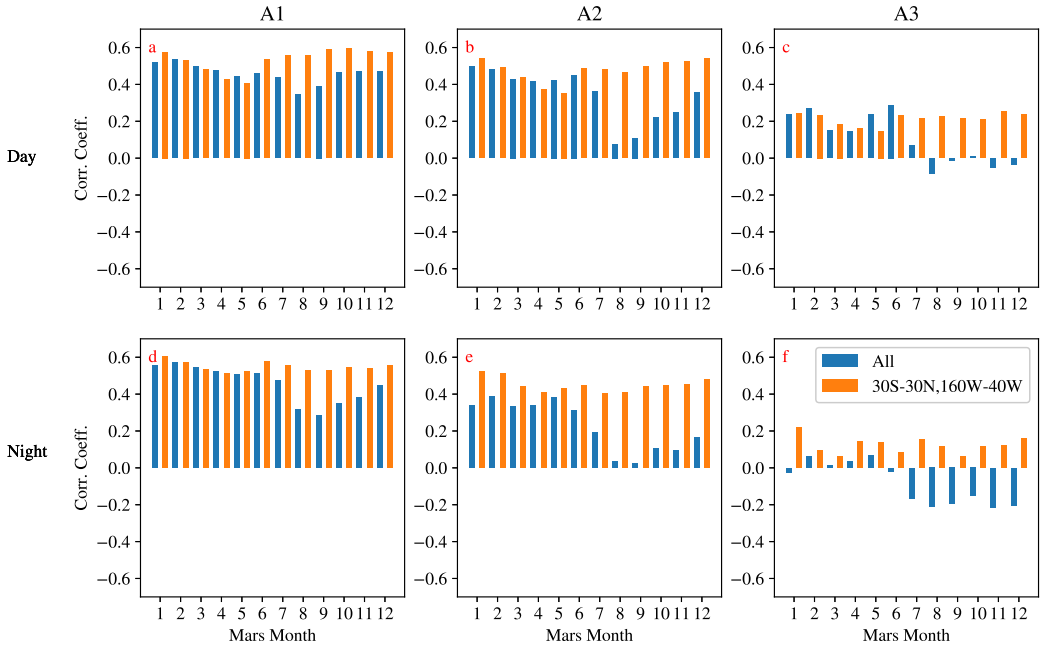

Figure 17. Correlation **product-moment** (weighted by cosine of latitude of the bin) between $\log_{10}$ of roughness (m^2) averaged at 1° and $\log_{10}\hat{\Omega_{GW}}$ (K^2 K^{-2}) averaged at 1° resolution for the channel, time of day, region, and Mars Month labeled. Mars Month is defined as L_s=0°–30° for Month 1 etc. Blue bars indicates the global correlation, while orange bars are for the region of Tharsis Montes and Valles Marineris 30° S–30° N, 160°–40° W

roughness more strongly correlates with GW activity at the low altitudes sensed by A1 and A2 in the nadir observations. **GW activity in A3 correlates or anti-correlates more strongly with elevation than roughness (Table 1).** In the off-nadir, elevation weakly correlates with GW activity in dayside A3 observations but nightside GW activity in A3 is poorly explained by roughness or elevation. In A1 off-nadir observations, surface roughness correlates more strongly with GW activity than elevation. The same is true in A2 on the nightside but not on the dayside (Table 1). Thus, the tropical GW population observed from the nadir appears to evolve with altitude from one correlated with surface roughness to one correlated or anti-correlated with elevation, whereas the GW population observed from the off-nadir appears to evolve with altitude from one correlated with roughness to one independent of surface roughness or elevation.

However, correlation between the logarithm of surface roughness and logarithm of GW activity in A1 does not seem as strong as inspection of the spatial distribution plots would suggest. One way to understand this is look at the set of one-dimensional probability distribution functions of GW activity within each discrete interval of surface roughness (again on logarithmic scales) and how they change with surface roughness, as in Figs. 18a–b. First, the most probable values of GW activity (the brighter colors) only correlate strongly with roughness at roughness $> 10^5$ m^2. Below this value, there may be some weak correlation between surface roughness and GW activity, but surface roughness and GW activity are certainly independent at surface roughness $< 10^3$ m^2. Second, the probability distribution functions are quite broad. Below the range of roughness where surface roughness and GW activity strongly correlate, the minima of the distributions are flat near $\hat{\Omega_{GW}} = 10^{-7}$ K^2 K^{-2}, which is approximately the characteristic uncertainty in individual diagnoses of GW activity (assuming a variance of 0.005 K^2 at 170 K: Heavens et al. (2020)), while the maxima of the distributions increase with a slope with an exponent < 1. In the region where surface roughness and GW activity strongly correlate, the minima of the distributions generally increase along the same slope as the center of the distribution, while the maxima of the distributions flatten. So depending on how the widths of the distributions are measured, areas with the same roughness can experience an order of magnitude of variability in GW activity or more.

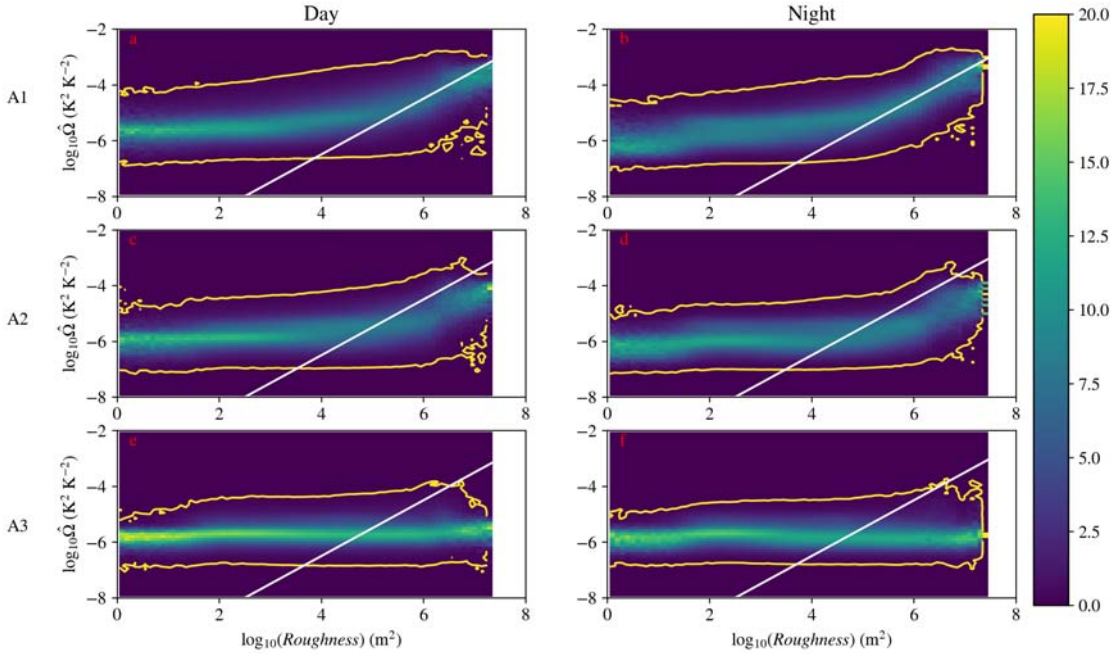

Figure 18. Normalized empirical probability density functions (%) of $\log_{10}\hat{\Omega_{GW}}$ (K^2 K^{-2}) in discrete $\log_{10}$ of surface roughness (m^2) bins for all off-nadir observations at surface elevations < 12 km and MY 29–33,35 for the channels and times of day listed. For clarity, the colorscale has been saturated at 20%. The 0.1% probability contour is plotted in yellow to indicate the extremes of the distributions. The white line indicates a possible linear relation between $\log_{10}$ of roughness (m^2) and $\log_{10}\hat{\Omega_{GW}}$, i.e., $\log_{10}\hat{\Omega_{GW}}$=$\log_{10}(roughness)$-10.5

Where the logarithms of roughness and GW activity in A1 do correlate strongly, the slope of their relationship is approximately 1, indicating that surface roughness and GW activity are linearly proportional over the roughest surfaces (Figs. 18a–b). This is expected behavior for orographic GW, as outlined by Creasey et al. (2006), which noted that orographic GW schemes used the surface wind stress as a proxy for orographic GW activity by relating surface wind stress to the vertical flux of horizontal momentum, absent dissipation. For A1, GW are presumably being observed close to their sources under conditions of near-perfect visibility (Fig. 6a,d). In that case, the expected relationship between surface roughness and $\hat{\Omega_{GW}}$ in A1 (assuming 100% visibility) can be derived by combining Eq. 7 of Ern et al. (2004) with Eq. 2 of Creasey et al. (2006):

$$\hat{\Omega_{GW}} = \frac{2\kappa N^3 U}{g^2}\frac{\lambda_h}{\lambda_z}\sigma_t^2 \tag{4}$$

where κ is a "tunable parameter" of 10^{-4} m^{-1} in Creasey et al. (2006), U is the wind velocity, g is the gravitational acceleration, and σ_t^2 is the surface roughness.

If we estimate $\frac{\lambda_h}{\lambda_z}$ to be 1.5–3, N as $\approx 8{\times}10^{-3}$ s^{-1}, the expected magnitude of the term on the r.h.s. of Eq. 4 multiplying surface roughness is 1–2 $\times 10^{-11}U$. The fit by inspection in Figs. 18a–f suggests a value of $\approx 3 \times 10^{-11}$ for this term, which implies typical surface winds of 1.5–3 ms^{-1}. Note that κ in Creasey et al. (2006) has physical meaning taken from Palmer et al. (1986) and Lewis et al. (1999), where it is a characteristic horizontal wavenumber, k_h. However, Lewis et al. (1999) seems to have omitted a factor of $\frac{1}{2}$ included by Palmer et al. (1986). And so κ is at most 7.5×10^{-5} m^{-1}–1.5×10^{-4} m^{-1} to align with the sensitivity of A1 off-nadir observations.

Potential variables other than the wind are constrained by a factor of 3 or better. Therefore, the scatter around the fit line in Figs. 18a–f is generated either by direct wind variability or because the local wind and stability conditions lead to topography obstructing rather than disturbing the circulation (Lott & Miller 1997). In the former "blocking" case, amplitudes are reduced by up to an order of magnitude from the expected linear wave solution (Lott & Miller 1997). For non-blocked waves, GW generation by surface winds of 30 ms^{-1} seems plausible in rare cases. The flattening of the

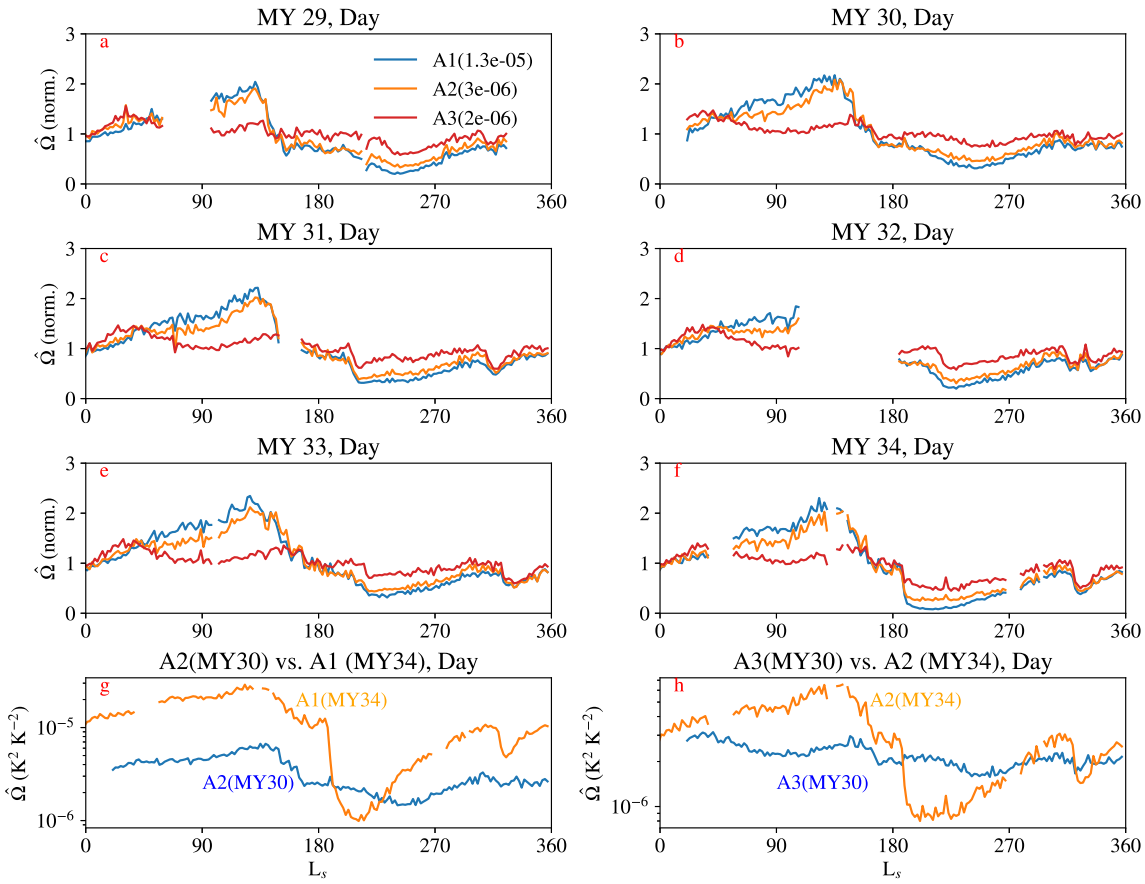

Figure 19. Seasonal variability in global mean GW activity on the dayside: (a–f): $\hat{\Omega_{GW}}$ (K^2 K^{-2}) filtered so that sum of the cosine of the latitude bins averaged to calculate the mean is at least 50 ($\approx$ 86% coverage) and normalized by the mean for all time bins for the channel. The normalization factor is given in the legend; (g–h): Comparison of the seasonal cycle of global mean dayside $\hat{\Omega_{GW}}$ (K^2 K^{-2}) in a channel during the dust storm-quiet year of MY 30 compared with the seasonal cycle of global mean dayside $\hat{\Omega_{GW}}$ during MY 34 in a second channel whose vertical range should correspond to the first channel under high dust opacity conditions, as labeled. **Note that 34P started around L$_s$=187°, MY 34.**

maxima of the distributions at high roughness implies that winds > 10 ms^{-1} over the roughest surfaces are generating waves with unstably high amplitudes. It is also possible that rough, low elevation surfaces like Valles Marineris have apparently higher levels of GW activity because they are observed somewhat higher in altitude relative to the surface than typical and the GW they excite have grown with amplitude over that altitude range.

Yet dissipation seems to outpace amplitude growth with decreasing density over the next two scale heights. In A2, surface roughness and GW activity correlate at higher surface roughness values, but GW activity is somewhat weaker in magnitude at high surface roughness, though similar in magnitude to A1 at lower surface roughness (Figs. 18c–d). In A3, surface roughness and the most probable values of GW activity are uncorrelated at all surface roughnesses. Even the maxima of the probability distributions are independent of surface roughness, though the maxima of the probability distributions at intermediate surface roughness are greater than the maxima at low and high surface roughness (Figs. 18e–f). The weaker amplitudes could be partly explained by the lower visibility of GW in A2 and A3, but the de-correlation between activity and roughness with altitude is positive evidence for dissipation.

The high degree to which variability in wind and stability likely drives topographic GW activity precludes isolating the topographic GW component of $\hat{\Omega_{GW}}$ from the non-topographic component in A1 or A2 observations to assess their spatial distribution without information about surface winds. But it is possible to argue from the independence of GW activity from surface roughness over areas with surface roughness $< 10^5$ m^2 and the unrealistic surface winds that would be implied by the GW activity observed over a smooth area that significant GW activity over smooth areas is non-orographic. For example, the GW activity of 10^{-5} K^2 K^{-2} in the areas with surface roughness $< 10^4$ m^2

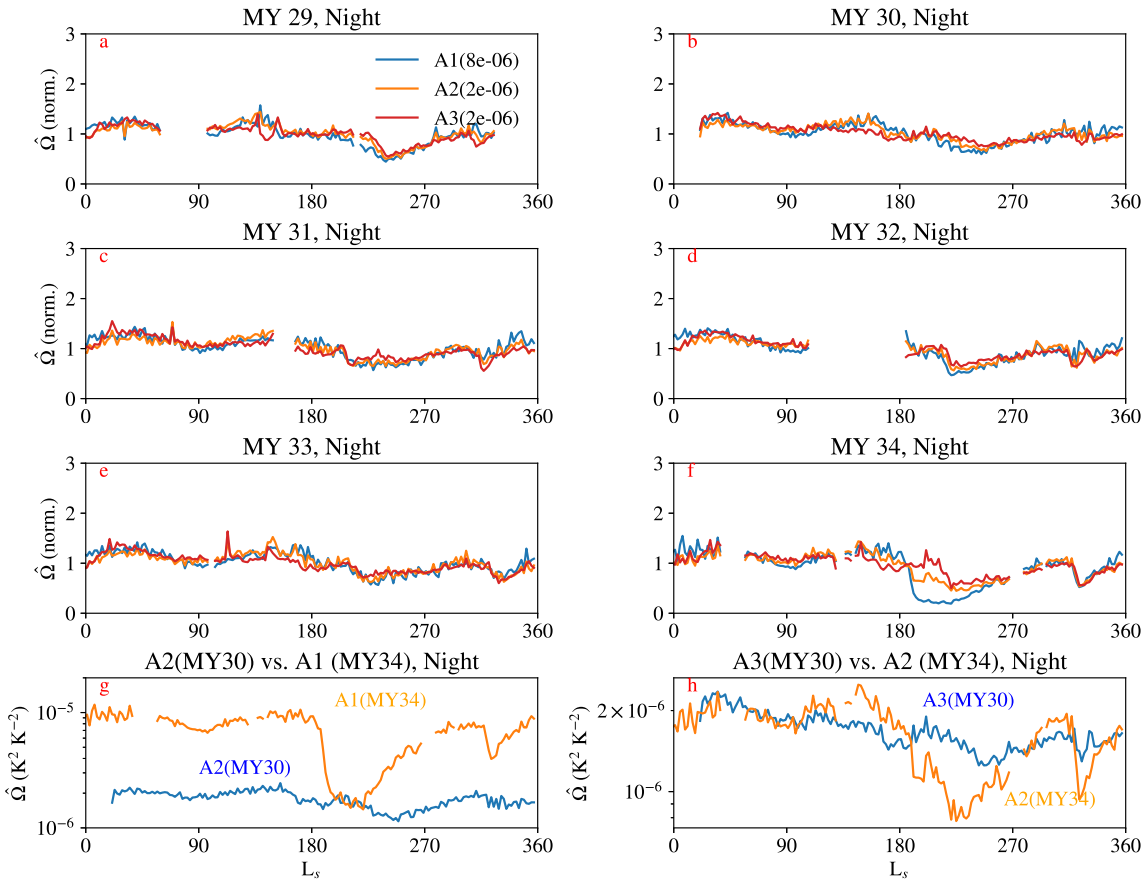

Figure 20. Seasonal variability in global mean GW activity on the nightside: (a–f): $\hat{\Omega_{GW}}$ (K^2 K^{-2}) filtered so that sum of the cosine of the latitude bins averaged to calculate the mean is at least 50 ($\approx$ 86% coverage) and normalized by the mean for all time bins for the channel. The normalization factor is given in the legend; (g–h): Comparison of the seasonal cycle of global mean nightside $\hat{\Omega_{GW}}$ (K^2 K^{-2}) in a channel during the dust storm-quiet year of MY 30 compared with the seasonal cycle of global mean nightside $\hat{\Omega_{GW}}$ during MY 34 in a second channel whose vertical range should correspond to the first channel under high dust opacity conditions, as labeled. **Note that 34P started around L_s=187°, MY 34.**

would require > 45–90 ms^{-1} surface winds (and no blocking), so GW activity observed in northern autumn and winter **(L_s=180°–360°) over smooth areas of the northern extratropics (e.g., most of the area in the 45–80° N band in** Figs. 14a–b) is likely non-orographic.

4.2. *Seasonal variability and dust storm activity*

Heavens et al. (2020) found that GW activity in A3 off-nadir views had a strong seasonal cycle, with a maximum in northern summer, a minimum in northern fall, and pronounced minima during regional and global dust storm activity. There is a similarly phased seasonal cycle in A1 and A2 as well, but it has a higher relative amplitude on the dayside in A1 and A2 than in A3 (Figs. 19a–f). The seasonal cycle of activity on the nightside is very similar in all three channels (Figs. 20a–f). The normalization factors suggest that GW activity is globally weaker at higher altitudes and globally stronger on the dayside than the nightside. Given that $\hat{\Omega_{GW}}$ should increase exponentially with altitude normalized by the scale height rather than decrease by a factor of 4, the differences in the normalization factors between the channels alone suggests there is strong dissipation of GW activity in the lower atmosphere. Accounting for the decrease in GW visibility in the channels, which is no more than a factor of 2 for the waves with wavelengths to which off-nadir observations are most sensitive, still would imply GW activity should increase by a factor of 2 between A1 and A3. And the strong contrast between the seasonal cycles of A1 and A2 and that of A3 on the dayside (Figs. 19a–f) suggests that GW activity experiences stronger dissipation in northern summer than in any other season.

And as in A3, GW activity in A1 and A2 seems to weaken during regional and global dust storm activity. This phenomenon can be seen most easily on the dayside during the C-type (in the sense of Kass et al. (2016)) regional

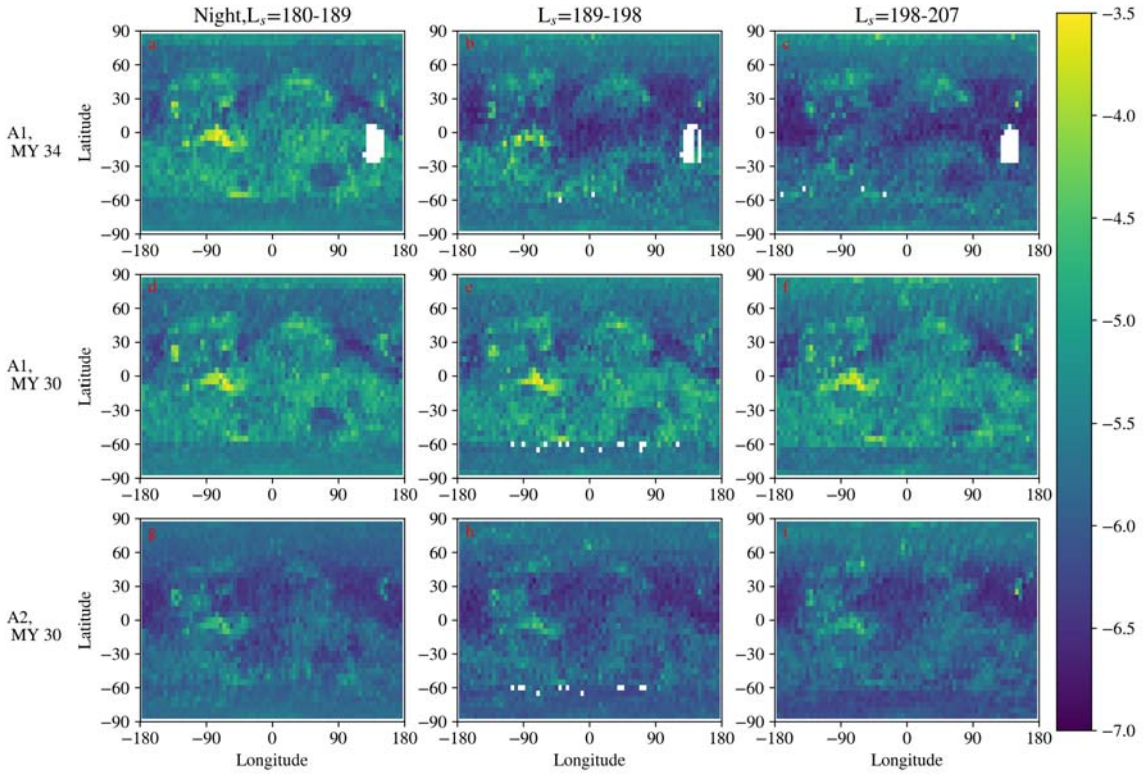

Figure 21. Mean spatial distribution of GW activity viewed from nightside off-nadir observations averaged at 5° resolution expressed as $\log_{10}\hat{\Omega_{GW}}$ (K^2 K^{-2}) for the channel and time interval labeled in order to compare A1 GW observations during the MY 34 global dust event with A1 and A2 observations during the dust storm-quiet year of MY 30. White space indicates that no data is available in the averaging bin. The lower end of the plotting colorscale is saturated at 10^{-7} K^2 K^{-2}, the approximate uncertainty in the planet's coldest areas (the winter polar cap).

dust storms toward the end of northern winter (L_s=300°–330°) in MY 29, MY 31–34 (Figs. 19a,c-f) but is present in other large regional dust storms and 34P, which started just after northern fall equinox **(L_s=187°)** (Fig. 19f). One explanation for the minima in GW activity during dust storms would be observational. As discussed in Section 2, dust opacity raises the altitude to which on-planet views in A1–A3 are sensitive. A1's weighting function and the visibility of GW to observations under high dust opacity resemble those of A2 under normal conditions. A2's weighting function and the visibility of GW to observations under high dust opacity resemble those of A3 under normal conditions (Figs. 2a–i). And the altitude of the peak of A3's vertical weighting function rises by ≈ 10 km under high dust opacity. Given that GW activity is strongly dissipated in the lower atmosphere and peak visibilities seem to decrease with altitude, raising the vertical range of sensitivity of the channel would result in a lower magnitude of GW activity being observed, all else being equal. But if the near-surface GW sources were unaffected by the dust storm, we likewise would expect the magnitude of GW activity observed in A1 and A2 to be similar to that observed in A2 and A3 under normal conditions.

However, in most cases, the global mean GW activity observed during MY 34 in the channel with the lower altitude of peak sensitivity fell to a lower level than the channel with the higher altitude of peak sensitivity during the dust storm-quiet year of MY 30 (Figs. 19g-h; 20h). The one exception is nightside A1 during MY 34, when global mean GW activity fell to a level indistinguishable with A2 during MY 30 (Fig. 20g).

Yet the evolution of the spatial distribution of GW activity at night as 34P developed is inconsistent with A1 during the dust storm sampling the same GW distribution as A2 during normal conditions. In the period before 34P expanded to regional scale, nightside GW activity in A1 was nearly indistinguishable between MY 34 and MY 30 (Figs. 21a,d).

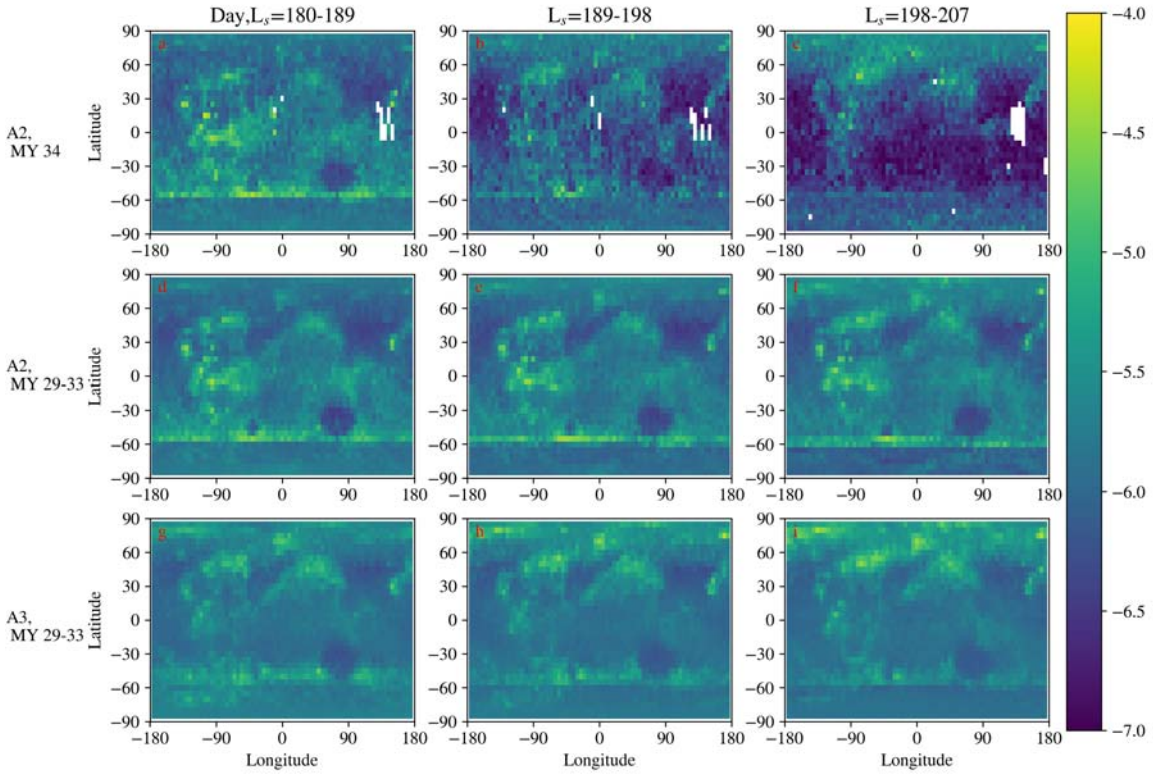

Figure 22. Mean spatial distribution of GW activity viewed from dayside off-nadir observations averaged at 5° resolution expressed as $\log_{10}\hat{\Omega_{GW}}$ (K^2 K^{-2}) for the channel and time interval labeled in order to compare A2 GW observations during the MY 34 global dust event with A2 and A3 observations during the dust storm-quiet year of MY 30. White space indicates that no data is available in the averaging bin. The lower end of the plotting colorscale is saturated at 10^{-7} K^2 K^{-2}, the approximate uncertainty in the planet's coldest areas (the winter polar cap).

In the next period, as 34P expanded from regional to global scale, GW activity decreased in the tropics and in some smoother mid-latitude areas relative to MY 30 (Figs. 21b,e). And as 34P peaked in intensity (see Heavens et al. (2019)) during the next period, the spatial distribution of GW activity in A1 somewhat resembled that of A2 during MY 30 (Figs. 21c,i). But GW activity in A1 was somewhat weaker in smoother areas and Valles Marineris than A2 during MY 30 (e.g., Hellas) but somewhat stronger in a region running to the NE of Valles Marineris toward the typical hotspot of GW activity near 30° N, 60° E.

And in the case of A2 and A3 on the dayside, where global mean GW activity during MY 34 in A2 fell below global mean GW activity in A3 during MY 30, the spatial distribution of GW activity during 34P evolves to contrast more strongly with A3 during MY 30 by L$_s$=198°–207° (Figs. 22c,i). GW activity is much weaker in A2 than A3 except in a few hotspots in the northern mid-latitudes and an area NE of the Tharsis Montes (0°-30° N, 90° W).

This last area (particularly near Fortuna Fossae) also was identified by Heavens et al. (2020) as an area of unusually high GW activity during 34P. Dayside GW activity in this area does not correlate strongly with roughness in this area (Fig. 23a). In addition, it would require surface winds of at least 45–90 ms^{-1} to generate $\hat{\Omega_{GW}}$ in A1 of 10^{-5} K^2 K^{-2}, a level of activity typically observed during most of the year (Fig. 23b). Therefore, significant GW activity observed in this region is almost certainly non-orographic.

GW activity in A1 around L$_s$=200° here was slightly higher than was typical at this season during the other MY but much below the level sometimes observed during northern spring and summer (Fig. 23b). GW activity in A2 around L$_s$=200° of MY 34 was similar to that observed in A2 during northern spring and summer (Fig. 23c), while GW activity around L$_s$=200° of MY 34 exceeded GW activity in northern spring and summer by a factor of 3–7. Thus,

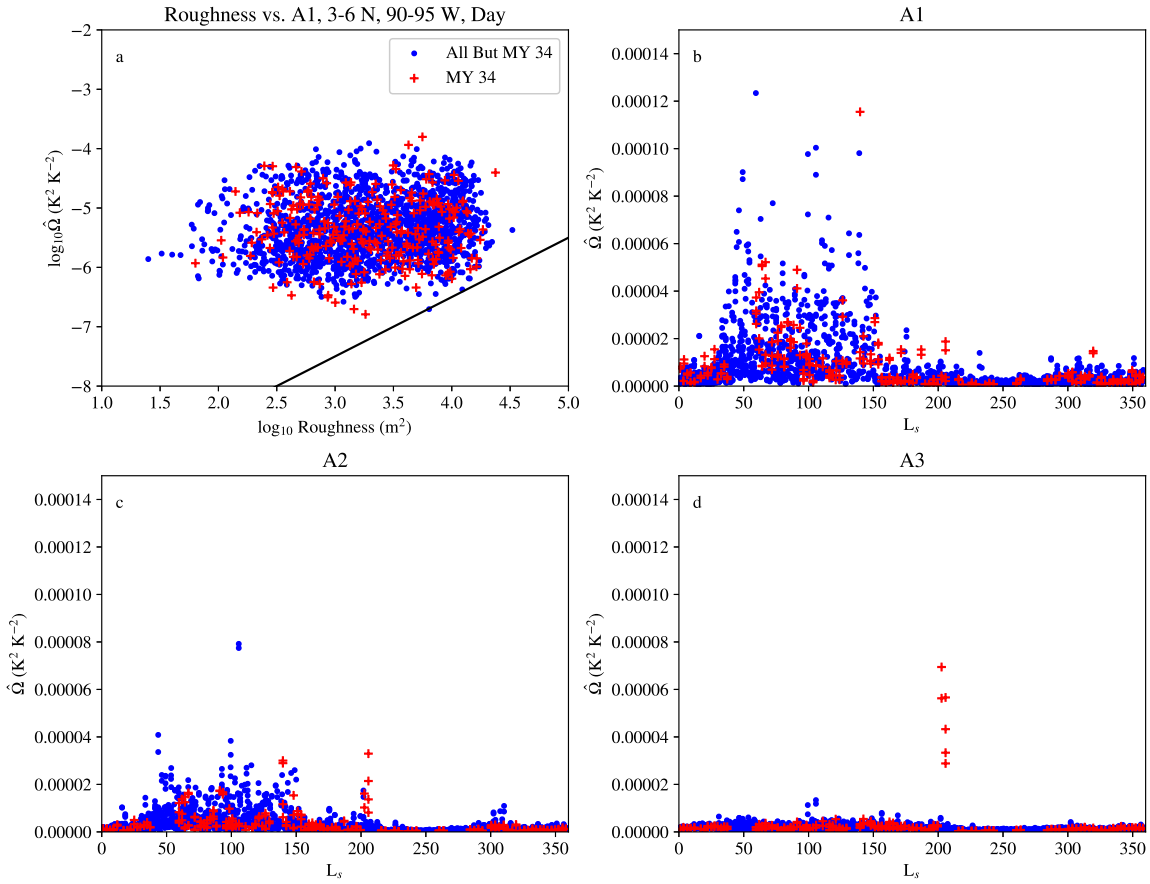

Figure 23. Dayside GW activity during 34P near Fortuna Fossae and its context: (a) $\log_{10}(roughness)$ (m^2) vs. $\log_{10}\hat{\Omega_{GW}}$ (K^2 K^{-2}) for all dayside A1 off-nadir observations with maximum surface elevations < 12 km in 3°–6° N, 90–95° W. The black line indicates $\log_{10}\hat{\Omega_{GW}}$=$\log_{10}(roughness)$-10.5; (b) $\hat{\Omega_{GW}}$ (K^2 K^{-2}) for all dayside A1 off-nadir observations with maximum surface elevations < 12 km in 3°–6° N, 90–95° W; (c) same as (b) but for A2; (d) same as (b) but for A3. Blue dots indicate observations in years other than MY 34 and red crosses indicate observations during MY 34.

GW activity observed in this region typically decreases by an order of magnitude in the roughly two scale heights between the peak sensitivity of A1 and A3 (Fig. 2). But the GW activity observed around L_s=200° of MY 34 was unusual in growing substantially over the same vertical range.

Inspection of the individual observations, including the pair with highest A3 variance in Fig. 23d and the adjacent pair, suggests the GW activity here is not an artifact. The first pair of A1 observations cools with increasing distance (and increasing altitude as the observation is advancing across the array from detector 21 to detector 1) (Fig. 24a), which implies a steep lapse rate. This steep lapse rate is also inferred from the first two observations in A4 (centered at 843 cm^{-1}), A5 (centered at 463 cm^{-1}), and B1 (Figs. 24d-f). Normally, these channels are used to retrieve water ice, dust, and surface temperature respectively (Kleinböhl et al. 2009, 2011) but likely gained dust opacity and thus stronger sensitivity to lower atmospheric temperatures during the dust storm. The second pair of observations in A1 departs from a straight line form at the ends of the observations, suggesting a low amplitude wave is mixed with the steep decrease in temperature with altitude (Fig. 24a). This pair of observations looks similar in A5, only 4 K warmer (Fig. 24c). The first two observations in A2 likewise bend at the lower end, while the second two observations bend at both ends (Fig. 24b). But it is in A3 that the waves become most pronounced (Fig. 24c). The observations in the different channels are not observing the exact same place but do seem to observe growing wave activity from the lower atmospheric opacity channels of B1, A4, and A5 (in that rough order) through A1, A2, and A3. None of the activity observed has unusually low brightness temperatures in the first few detectors, which is the most typical artifact in MRO-MCS on-planet radiance observations.

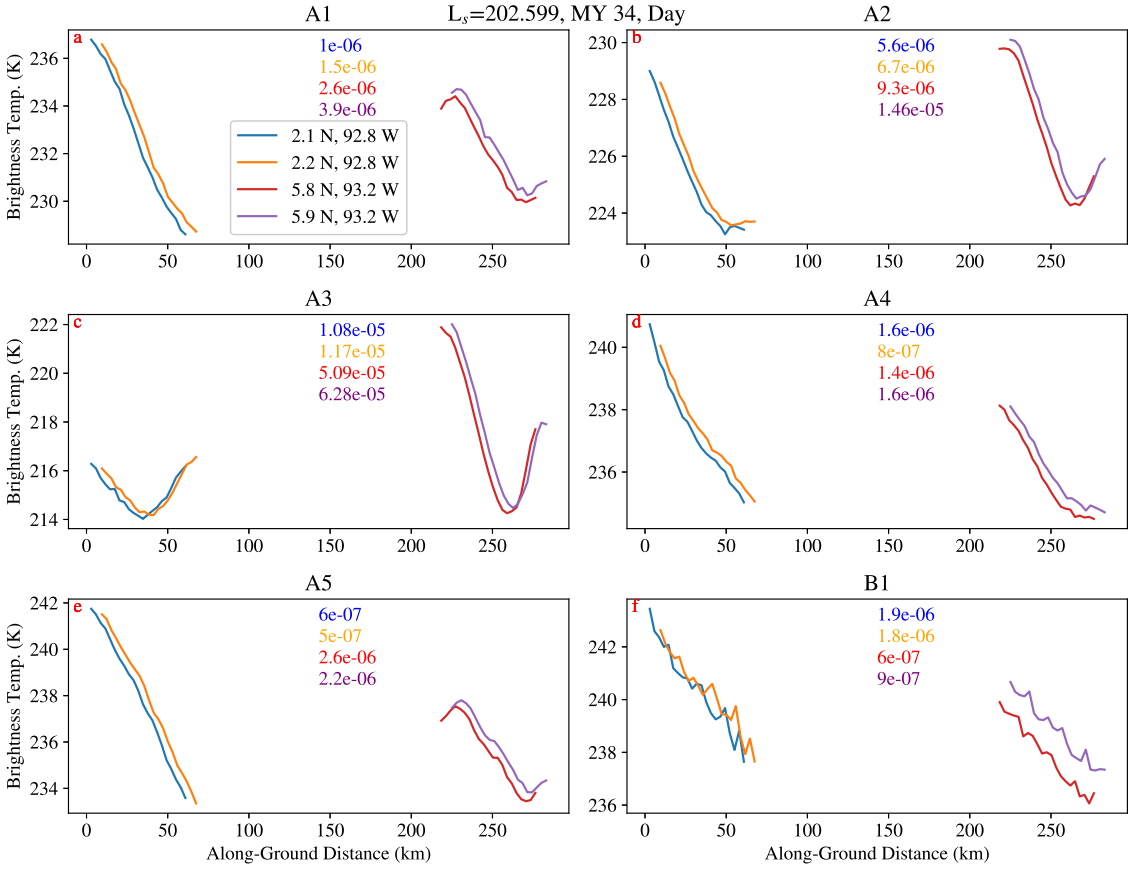

Figure 24. Example calibrated radiance observations near Fortuna Fossae during 34P for the labeled channels and locations. The corresponding $\hat{\Omega_{GW}}$ (K^2 K^{-2}) for these observations is provided by color-coded text within the panels. The observations are plotted based on the intersections of each detector with the surface and relative to the intersection with the surface of detector 21 of the first observation.

The increase in GW activity between A1 and A3 is a factor of 10–20, greater than the factor of e^2 that would be expected for conservative growth of a GW with height, especially with a scale height of $\approx$ 11 km implied by the observed brightness temperatures. (Recall that GW amplitude increases in proportion to $exp(\frac{z}{2H})$, so $\hat{\Omega_{GW}}$ increases in proportion to $exp(\frac{z}{H})$.) One explanation is that the relationship between GW energy and $\hat{\Omega_{GW}}$ is such that increasing N^2 for constant energy will increase $\hat{\Omega_{GW}}$ linearly. This seems unlikely. Stability seems to have decreased with altitude from the lower to the middle atmosphere in the tropics during 34P (Heavens et al. 2019). Another possibility is that additional GW are being generated between the level of A1 and A3. A third explanation is that meridional wind speed significantly changes between A1 and A3, changing the intrinsic phase speed of the wave (and thus its vertical wavelength) so that GW are more visible. The principal meridional overturning circulation long has been simulated to intensify substantially during dust storm activity (e.g., Wilson 1997), and there is evidence for extremely rapid cross-equatorial advection of dust in the early stages of 34P (Shirley et al. 2020) and a few hundred km to the west of Fortuna Fossae within a few sols of the GW observations in Figs. 24a–f.

Distinguishing between intrinsic phase speed change and additional GW generation is not straightforward. Assuming the second pair of observations for A1–A3 and A5 captures the peak and trough of a single wave implies an apparent horizontal wavelength of 80–100 km (Figs. 24a–c,e). The horizontal alignment of the negative phase of this wave near 270 km shifts by $\approx$ 18 km between A1 and A3, implying a vertical wavelength of 50–65 km. A wave like this would be just on the edge of visibility (Fig. 6) and would not gain significant visibility by decreasing in vertical wavelength.

Thus, we are restricted to concluding that GW near Fortuna Fossae around L_s=200° were non-orographic and grew with height atypically for GW observed in this area outside 34P as well as atypically for GW in general. Given

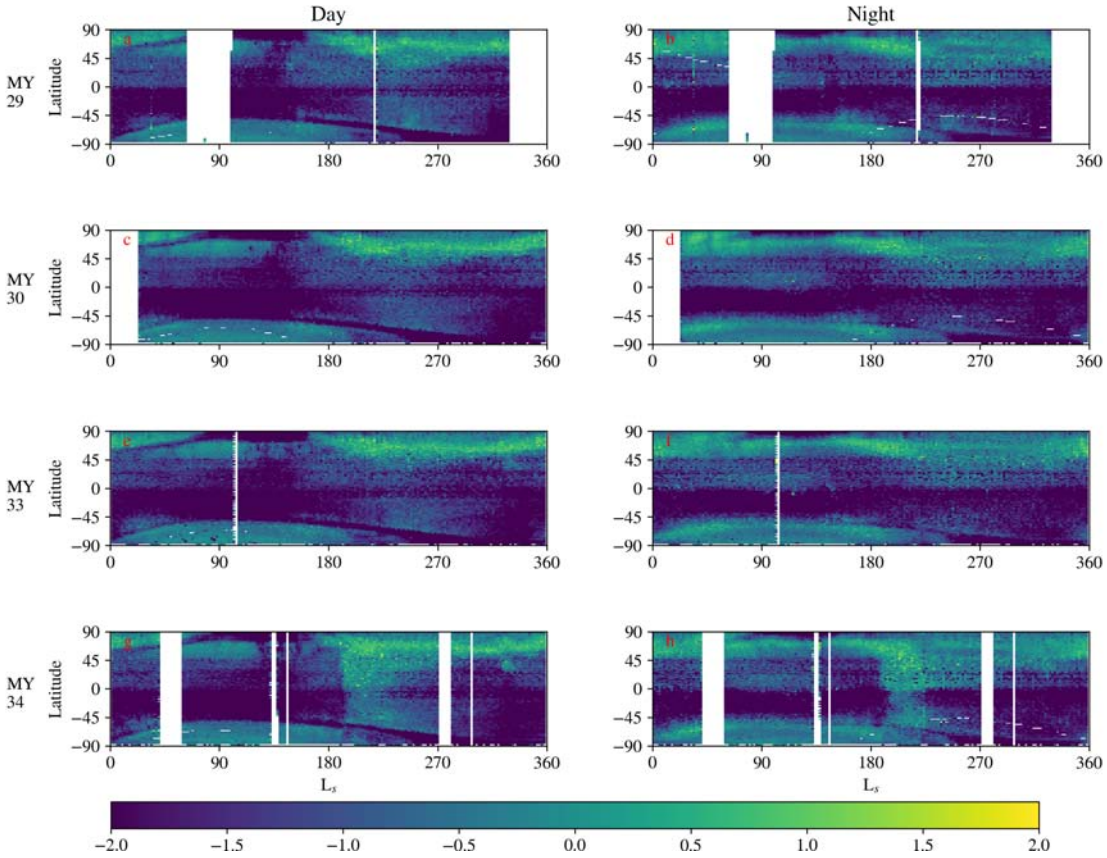

Figure 25. Natural logarithm of the ratio between zonal mean $\hat{\Omega_{GW}}$ (K^2 K^{-2}) in A3 and A1 for the MY and times of day labeled. **The scales are saturated at e^{-2} to indicate high dissipation and e^2 to indicate zero dissipation under ideal circumstances (no filtering). Dark/blue colors thus indicate high filtering and light/yellow colors thus indicate low filtering.** White space indicates missing data.

non-linear growth of the apparent disturbance with decreasing density, critical level filtering of GW and other GW dissipation with altitude (hereafter filtering) here must have been minimal.

By taking the ratio of zonal mean GW activity between A3 and A1, it is possible to investigate how GW activity grew or did not grow with height and thus the extent of filtering on a more global scale (Figs. 25a–h). Filtering of GW seems to have been minimal throughout the tropics during 34P. Under normal conditions, gravity wave activity is least filtered in the winter extratropics, moderately filtered in the summer extratropics, strongly filtered in the northern tropics and in the southern tropics during southern spring and some of southern summer, and almost completely filtered in polar day and in the southern tropics during southern autumn and winter (Figs. 25a–f). During 34P, filtering in the tropics weakened to levels similar to that of their respective extratropics. If GW dissipation were weaker below ≈ 15 km as well as between ≈ 15–35 km, the reduction in GW activity in A1 during 34P by an order of magnitude on the dayside (Fig. 19g) could not be explained by A1 observing higher in the atmosphere and with lower visibility to GW, which would explain a factor of 2 decrease at most.

4.3. *Tropical nightside activity: a carbon dioxide ice cloud artifact?*

The GW activity in the tropics observed in A3 off-nadir observations on the nightside during the less dusty half of the year by Heavens et al. (2020) was distinctive because of the contrast in the magnitude of GW activity between day and night and the high intermittency of GW activity in some areas of the tropics. That is, there were a relatively few number of observations with extremely high variances. Heavens et al. (2020) considered whether this result could arise from re-emission by absorbing mesospheric CO_2 clouds with cloud particle grain sizes ≤ 1 μm. Having found

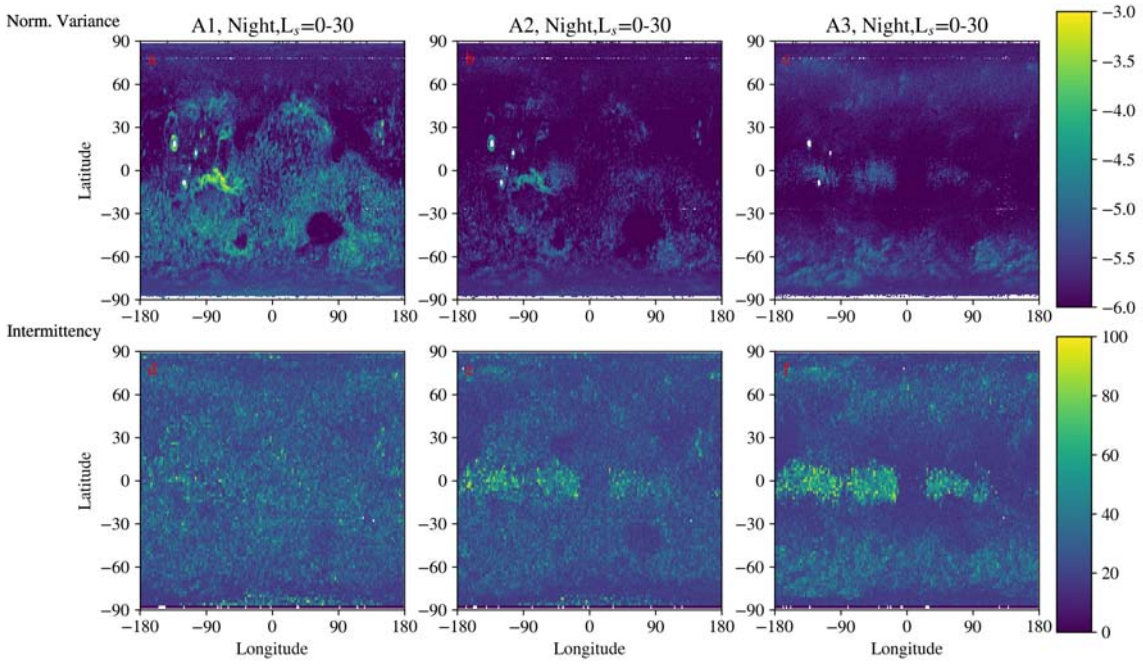

Figure 26. Nightside gravity wave variability and intermittency at L_s=0–30°: (a–c) $\hat{\Omega_{GW}}$ (K^2 K^{-2}) averaged at 1° resolution for all off-nadir observations at surface elevations < 12 km and MY 29–33,35 for the labeled channel; (d-f) Intermittency (%) at 2° resolution for the labeled channel. The difference in resolution is to ensure sufficient sampling to reliably calculate intermittency.

that high variances in this location and season were always observed in association with "loop features" indicative of clouds, Heavens et al. (2020) suggested that clouds with nadir optical depths in A3 of > 0.02 could be responsible.

If these clouds did consist of sub-micron particles, their signal should be limited to A3. Modeling by Hayne et al. (2012) (see Fig S3 of Heavens et al. (2019)) showed that the extinction coefficient, Q_{ext} of a CO_2 ice particle ≤ 1 μm was an order of magnitude higher in A3 than A2. And because the variance due to re-emission scales with the optical depth and thus Q_{ext} for largely absorbing particles for optical depth $<< 1$ (Heavens et al. 2020), the variance artifact introduced by such a cloud would be two orders of magnitude less in A2 than in A3 (and even smaller in A1 by a similar chain of reasoning). However, Fig. 26a–f shows normalized variance and intermittency in A1, A2, and A3 on the nightside during L_s=0–30°, the most active period for this apparent nightside GW activity. Areas of the tropics can be identified with similar levels of normalized variance in both A2 and A3 and high intermittency. In A2, these areas of high normalized variance tend to blend into the high activity associated with Valles Marineris and other topographic features, but the spatial distribution of intermittency in the tropics is quite similar between A2 and A3 (Figs. 26e-f). Moreover, just to the east of Valles Marineris (near 45° W), the magnitude of GW activity is similar between A2 and A3 and easy to compare (Figs. 26b-c). These areas of activity are absent in A1 (Figs. 26a,d).

In some cases, it is possible to show that substantial A1–A3 variance in the off-nadir is directly attributable to a CO_2 ice cloud. Fig. 27 shows a thorough breakdown of A1–A3 observations of a nightside loop feature near the Equator from northern summer of MY 34. Loop features have been interpreted to be discrete cloud layers whose true altitude is at the peak of the loop but are observed on either side of their true location as they rise and set with respect to the limb observation (Sefton-Nash et al. 2013). In this case, the curve of the loop seems to be interrupted at 5° S. Behind this feature, radiance in the lower detectors is anomalously low compared to the observations to the north and the south, because the cold, high altitude cloud is well forward of the tangent point. Thus, its emission is observed in preference to warmer emission from the surface (Figs. 27a–f). The profiles at the center of the loop suggest the presence of a cloud at 60 km altitude (Figs. 27d–f). (Observations like this are regularly used to detect polar stratospheric and polar mesospheric clouds on Earth, (e.g., Massie et al. 2007; DeLand & Gorkavyi 2021)).

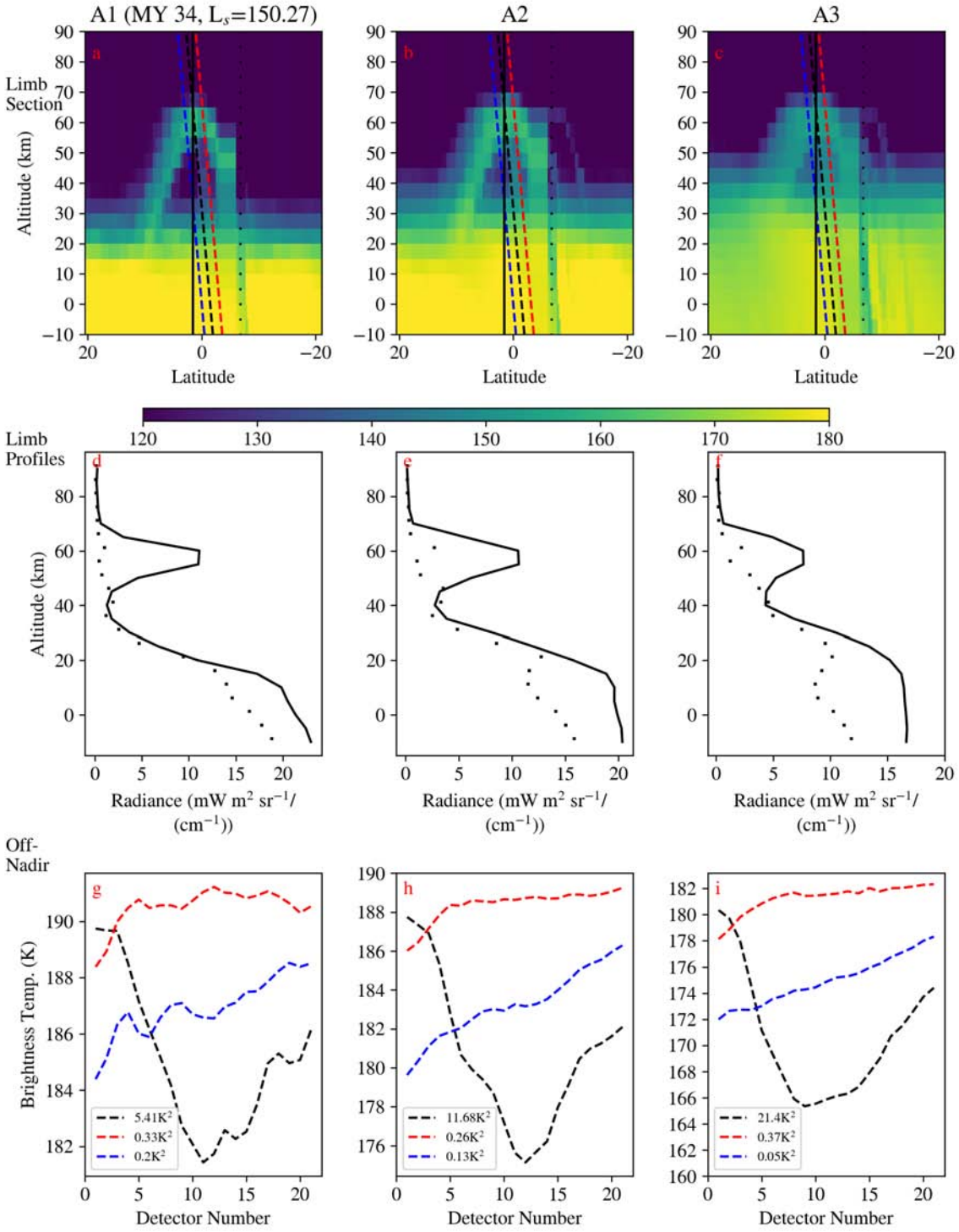

Figure 27. Limb and off-nadir observations of a loop feature/ presumptive cloud associated with high Ω_{GW} in A3: (a–c) Cross-sections of the brightness temperature in the labeled channel near 43° W, MY 34, L_S=150.27 (28 March 2018, 07:45–07:59 UTC). The color scale has been saturated at 120 K and 180 K to emphasize the loop feature. The latitudes of limb observations (at the tangent point of each detector) are indicated with horizontal lines in panels d-i, while the latitudes of off-nadir observations are depicted with slanted lines to show the projected observational path of off-nadir observations relative to the limb observations. The latitude axis has been reversed to show that the direction of spacecraft motion is toward the southern pole; (d-f) Comparison of two limb observations in the labeled channel. The dashed line plots a profile near the peak altitude of the loop. The square markers plot a profile in the shadow region on the far side of the loop feature from the spacecraft; (g-i) Off-nadir observations in the labeled channel, contrasting a high Ω_{GW} observation (one of a pair) with observations from the pair to the south and the north. Ω_{GW} for the observation is provided in the legend.

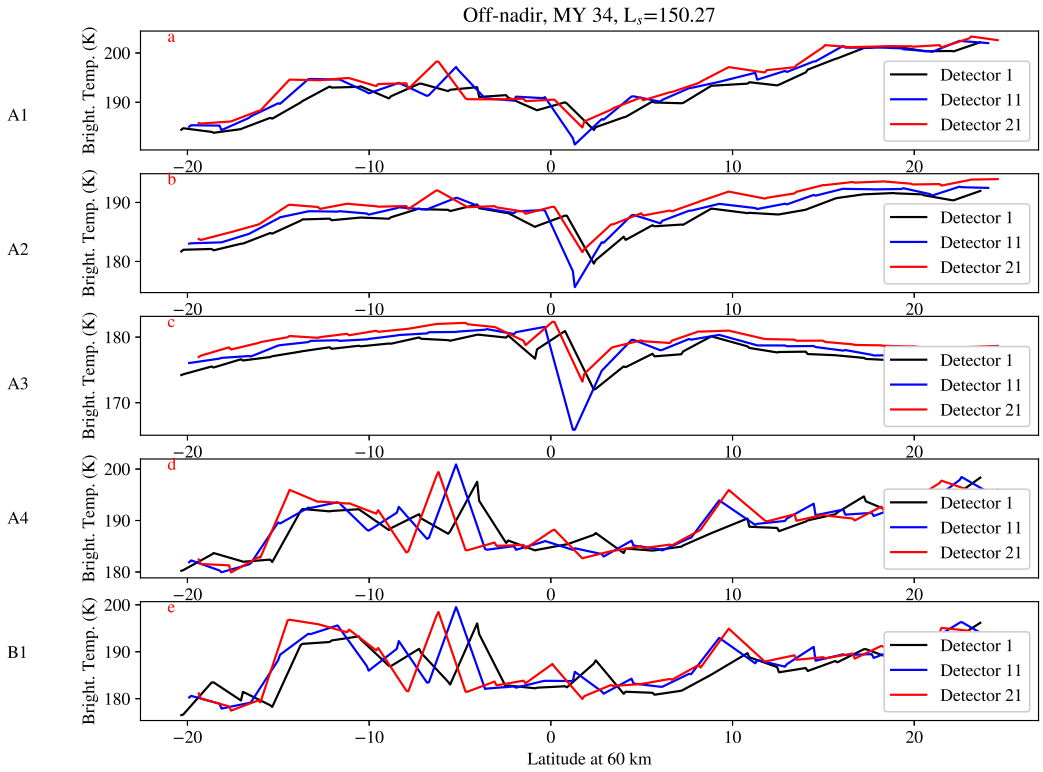

Figure 28. Off-nadir observations of a loop feature/ presumptive cloud associated with high Ω_{GW} in A3. Each panel shows brightness temperature measured by the labeled detectors in the labeled channel during a portion of an MRO orbit near 43° W, MY 34, L_S=150.27° (28 March 2018, 07:45–07:59 UTC). The latitudes of the observations have been shifted to correspond to where the path of the off-nadir observation would cross 60 km altitude, the estimated altitude of the cloud.

Off-nadir observations near this loop feature enable its extent along the direction MCS is observing to be quantified more precisely than is possible in limb observations, where the loop feature extends ≈ 18° (≈ 1000 km). One pair of high variance off-nadir observations intersects the surface near 1.5° S and show 8–12 K depressions in brightness temperature near the center of the observation and decreasing temperature across the observation (that is, from detector 1 to detector 21) (Figs. 27g–i). This decrease in temperature contrasts with the slight increase in temperature across the detectors in the neighboring observations and is strongest in A3. The importance of this pair of observations is clear when their observational paths are projected toward the spacecraft. These observations would intersect the peak of the loop feature at 60 km altitude and 1.5° N (Figs. 27a–c), whereas the neighboring observations would be 1–1.5° (60–90 km) to the north and south. That the depression in brightness temperature does not cover the full off-nadir observation that intersects the cloud also implies the cloud is < 60 km in width in the direction MCS is observing.

With its strong signal in A1–A3 (and moderate–strong signals in all of the other thermal infrared channels, which are not shown here), the loop feature in the limb can be interpreted as a strongly scattering CO_2 cloud at 60 km with particle size of > 5 μm, based on modeled extinction coefficients reported in the supplementary material of (Heavens et al. 2019). The strong signals in off-nadir observations in A1 and A2 as well as A3 are consistent with this idea (Figs. 28a–c). This signal is absent in A4 and B1 off-nadir observations, which resemble one another (Figs. 28d–e). CO_2 ice is relatively transparent in B1, but A4 has a similar extinction coefficient to A1 at CO_2 particle size > 5 μm. The single scattering albedo in A4 at 5–6 μm is ≈ 0.999 and 0.982 for A1 (Hayne et al. 2012), which suggests the A1 and A4 observations of CO_2 ice particles of ≈ 5 μm should be broadly similar. The simplest explanation of the discrepancy would be that the cloud was narrow enough cross-track to be missed by A4, which is the rightmost A

channel (the most western on the nightside) (McCleese et al. 2007). Thus, off-nadir views in A4 likely observed the same surface emission observed by B1, but the cloud was thick enough to allow some emission contribution in A1.

CO_2 particle sizes > 5 μm have been inferred from nightside loop features by Clancy et al. (2019). The nightside loop feature in Fig. 24 of Clancy et al. (2019) is impressive, but it is only evident in the off-nadir in a pair of off-nadir observations with A3 brightness temperature depressions of ≈ 2 K; this signal is minimal or absent in all other channels. Indeed, A4 agrees with B1 within ≈ 1 K (not shown). But it should be noted that the horizontal path length through the cloud (and thus the opacity) is at least an order of magnitude higher in the limb than the off-nadir, so two optically thick clouds in the limb could have much different off-nadir opacities. And if the cloud in Fig. 24 of Clancy et al. (2019) is thin enough, its small effect on A3 could translate to effects indistinguishable from noise in other channels. Thus, the imperfect correspondence between high off-nadir A3 variance and loop features in the limb reported by Heavens et al. (2020) for a sample of tropical nightside data probably can be explained by similar variability in cloud optical thickness.

5. DISCUSSION

In Section 1, we identified three key questions to be addressed by a more thorough study of GW activity in on-planet observations by MRO-MCS. Here, we will focus on these questions, briefly summarizing the key results, evaluating related questions that arose from the analysis, and considering the broader implications for understanding GW activity in Mars's atmosphere.

5.1. *Gravity wave activity changes during dust storm activity*

As outlined in Section 4.2, GW activity throughout the lower atmosphere largely decreases during regional and global dust storm activity. Even compensating for the potential change in the altitude to which particular channels are sensitive to GW, GW activity (in terms of a quantity proportional to GW potential energy) decreased by approximately a factor of 2 during 34P (Figs. 19–20). Heavens et al. (2020) noted that this decrease primarily occurred in areas of low–moderate activity in A3, but it is more precise to say that the decrease during 34P was largest in the northern tropics, moderate in the southern tropics and mid-latitudes, and largely absent in the northern extratropics **(both mid-latitudes and near the poles)** generally. Moreover, the decrease seems to have been larger on the dayside than the nightside (Figs. 21–22).

Even under mature dust storm conditions, GW activity in the lowest two scale heights during 34P remained high in Tharsis and just to its east (Fig. 22c). Unusually, GW activity in a smoother part of this region was far less attenuated than normal by the time it reached the 30–40 km altitude range sampled by A3 under dust storm conditions (Fig. 23d). However, attenuation of GW activity throughout the tropical lower atmosphere was weaker during 34P than any other time in the record (Figs. 25g–h), so local enhancement in GW activity here could originate as easily from a near-surface source unaffected by 34P as one specific to the event, such as one connected to the persistent, anomalously dusty mesoscale circulation(s) to the east of Tharsis inferred by Heavens et al. (2019)

High-resolution global climate modeling by Kuroda et al. (2020) reproduced the global reduction in GW activity, disproportionate reduction in the tropics and the southern extratropics relative to the northern extratropics, and improved GW vertical propagation conditions during 34P. But this study also simulated that GW activity near Tharsis changed minimally. Kuroda et al. (2020) ran $1.1° \times 1.1°$ (67 km) resolution GCM simulations with a dust scenario based on 34P column dust opacity measurements (Montabone et al. 2020) and compared it to a simulation with a climatological 'low dust' scenario. Indeed, Kuroda et al. (2020) notes that the zonal average reduction in GW activity in their simulations is typically about a factor of 2, which is smaller than that found by Heavens et al. (2020). This difference is attributed to sampling of a longer horizontal wavelength portion of the spectrum by the GCM simulations. However, this analysis suggests that this difference plausibly arises from high dust opacity raising the sensitivity altitude range of the A3 channel, **such that the change in GW activity is more accurately assessed by comparing GW activity sampled by A3 under dust-free conditions with GW activity in A2 sampled under dusty conditions, which implies a lower reduction in GW activity than found by Heavens et al. (2020).** If Kuroda et al. (2020)'s simulations accurately diagnose the dynamics behind the GW activity reduction, the reduction arises from a weaker diurnal cycle of surface heating below the dust haze suppressing generation of GW from planetary waves and geostrophic adjustment generally. The minimal or small positive impact of 34P on northern extratropical GW activity is attributed to orographic GW sources, which are apparently less affected by the effects of high dust opacity, though it seems possible that the persistence of GW activity in the northern extratropics during

673 34P is the result of the robustness of the winter westerly jet, embedded baroclinic activity, and the polar vortex. The
674 observational test for this would be to look for changes in GW activity from a regional dust storm or PEDE that
675 significantly disturbed the polar vortex such as 26C (a regional dust storm in MY 26) or 28P (Wang 2007; Kass et al.
676 2016; Guzewich et al. 2016; Battalio & Wang 2020) rather than 34P, which minimally impacted 50 Pa temperatures
677 north of 60° N (Kass et al. 2020).
678 Kuroda et al. (2020) also notes that the longer horizontal wavelengths resolved by the simulations are much longer
679 than the expected scale of GW generated by dry convection, so while it is expected that higher dust opacity will
680 stabilize the atmosphere, suppress convection, and suppress convectively generated GW; the simulations are unable
681 to simulate this effect. The similarity in magnitude and spatial distribution in the reduction in GW activity between
682 observations at the shorter horizontal wavelengths sampled by MRO-MCS off-nadir views and those resolved by Kuroda
683 et al. (2020) seems to support the suppression of dry convection by 34P. The subtlety identified by the observations
684 analyzed here is that there is significant orographic GW activity near the surface at the observationally resolved scales
685 within the tropics (e.g., Valles Marineris), but activity in these locations, too, is significantly weaker during 34P, even
686 at night (Figs. 21c,f,i). This reduction likely stems from the suppression of dry convection, which normally generates
687 intense mesoscale winds along steep slopes in Valles Marineris and similarly rough areas and potentially substantial
688 orographic GW activity (Toigo & Richardson 2002; Rafkin & Michaels 2003; Michaels et al. 2006; Clancy et al. 2021).
689 The other prediction by Kuroda et al. (2020) that seems confirmed by this analysis is that dissipation of GW with
690 altitude would have decreased in the tropics, at least in the sampled vertical range of the lowest 3–4 scale heights.
691 The mechanism invoked is stronger jets and reduced critical level filtering. This change is analogous to the reduced
692 critical level filtering that takes place near the westerly jets in the mid-high latitudes as they strengthen in autumn
693 and winter. Recent modeling by Rajendran et al. (2021) has proposed that the westerly jet in the northern hemisphere
694 expanded toward the Equator during 34P, which would be consistent with the reduced critical level filtering we have
695 inferred.

696 ### 5.2. *Carbon dioxide ice clouds and other phenomena that might be mistaken for gravity waves*

697 As outlined in Section 4.3, highly intermittent GW activity in the nightside tropics in the clear season of the year
698 (L_s=330°–150°) are the artifact of re-emission by CO_2 ice clouds with larger particle sizes than assumed by Heavens
699 et al. (2020). These anomalies are detectable as depressions in off-nadir brightness temperature that are significant
700 in A1–A3 and are potentially removable by statistical techniques for outlier exclusion. Because tropical mesospheric
701 CO_2 ice cloud clouds are rarer, thinner, and have larger particle sizes on the dayside than the nightside (Clancy et al.
702 2019), these artifacts are probably of minimal importance outside the nightside tropics in the clear season.
703 While MCS observations cannot distinguish GW activity from CO_2 ice clouds in the nightside tropics, the formation
704 of these clouds is thought to be impossible without GW-driven thermal fluctuations (Listowski et al. 2014; Yiğit et al.
705 2018). Thus, the relative spatial distribution of GW activity at 60 km is probably captured by our analysis in the
706 nightside tropics, making even this artifactual information potentially useful for model validation.
707 Along with potential impacts from non-GW mesoscale variability above the surface, on-planet observations in A1 and
708 A2 have a large enough potential surface contribution to enable surface temperature/composition variability to resemble
709 GW activity (Figs. 1– 2), which suggests that caution should be exercised when interpreting A1 and A2 brightness
710 temperature variability in areas where surface temperature could be changing rapidly because of composition, such as
711 the southern summer polar cap (Titus et al. 2003; Piqueux et al. 2008).
712 Analogously, the correlation between A1 and A2 brightness temperature variability and roughness at higher values
713 of roughness poses an additional question: whether this relationship is due to balance between the momentum flux of
714 GW activity and the surface stress, that is, it is an indicator of significant orographic GW sources; or whether it arises
715 from roughly uniform surface temperature lapse rates being translated into the atmosphere by radiative-convective
716 processes. For example, if surface temperature uniformly increased or decreased with elevation, it is possible that:

717 $$\Omega_{GW} = \sigma_t^2 \Gamma^2, \tag{5}$$

718 where Γ is the lapse rate. In that case, Γ^2 is typically equal to 9×10^{-7} K^2 m^{-2} (assuming our fit by inspection
719 of the data and a typical temperature of 170 K) or 1×10^{-3} K m^{-1} (0.96 K km^{-1}). On one hand, this is a low, but
720 still plausible atmospheric lapse rate near the surface of Mars, where the dry convective lapse rate is approximately
721 4.5 K km^{-1}. On the other hand, low elevation surfaces do not seem to be monotonically colder or warmer on Mars.
722 Figs. A1d and A2d show a rough decreasing trend in B1 brightness temperature with elevation in nadir and off-nadir

views, but this relationship is not monotonic. Elevations close to 20 km can be as warm as elevations near 0 km or lower. Moreover, the trend in brightness temperature with elevation in A1 is positive in the nadir and insignificant in the off-nadir (Figs. A1a and A2a) with the same caveats about scatter.

Even on Earth, the free atmospheric lapse rate can be a poor approximation for the decrease in surface temperature and the near-surface air temperature with elevation because of preferential solar heating of slopes, drainage of cold air into valleys, and variations in surface cover by snow or vegetation (Minder et al. 2010; Pepin et al. 2016). On Mars, physical considerations suggest that departure of the decrease in surface temperature and the near-surface air temperature with elevation from the free atmospheric lapse rate should be more common. The surface energy balance is primarily controlled by radiative fluxes. Stronger radiative cooling at night at higher elevations likely drives katabatic flows down slopes all over the planet at night (Spiga 2011), while solar heating on mountain summits during the day and resulting high infrared surface fluxes drives anabatic flow up slopes during the day (Rafkin et al. 2002). Thus, mesoscale atmospheric circulations generally tend to equilibrate temperature gradients along slopes. It is thus more likely that a correlation between surface roughness and temperature variability at the surface or in the atmosphere arises from a correlation between mesoscale variability and rough surfaces then observation of variable topography in a region with a uniform lapse rate.

Another alternative explanation for the strong relationship between brightness temperature variance in A1 and surface roughness is inhomogenous heating of rough surfaces. A smooth surface of uniform composition will heat uniformly, but one with slopes will heat preferentially according to the orientation of the slopes relative to the Sun. Thus, greater surface temperature variability would be expected over rougher terrains during the day. At night, a similar effect might be caused by cliff and crater walls having higher thermal inertia than crater/cliff floors (Edwards et al. 2011).

To test the idea that observed variance in the lowermost atmosphere or at the surface might arise from inhomogenous heating/cooling of rough surfaces, the annual mean surface temperature field output by the KRC numerical thermal model from Kieffer (2013) was analyzed. The KRC model simulates the surface and sub-surface energy balance for Mars, accounting for slope (at model resolution), thermal inertia, albedo, insolation, and infrared downwelling radiation (Kieffer 2013). Analyzing the annual mean field allows constant factors of surface composition and morphology that might affect km-scale variability in surface temperature from variable factors like insolation and infrared downwelling radiation. Normalized variance on the approximate scale of the MRO-MCS off-nadir observations was estimated by: (1) dividing the 0.05° KRC model output into 1° × 1° bins, consisting of 400 data points each; (2) taking each of the 20 sets of 20 points running north–south in each bin at constant longitude, linearly detrending the surface temperature data for these points, calculating the variance, and normalizing by the square of the surface temperature to find the normalized variance for each set; and (3) averaging the normalized variances in each bin.

The resulting normalized variance field is in Fig. 29. Surface temperature variability because of surface inhomogeneities is highest along the southern rim of Argyre and along the dichotomy boundary to the northeast of Arabia Terra. Several additional features with high normalized variance in Fig. 29 have high normalized variance in A1 nightside, e.g. Fig. 13. But many features do not match. Moderate variance is predicted by KRC in the lower thermal inertia regions approximately spanning the tropics from 180° W–60° W and 30° W–60° E, but these regions are not clear features in Fig. 13. Normalized variance in A1 is also concentrated more strongly around the rims of the Tharsis and Elysium volcanoes (Fig. 13) than in KRC (Fig. 29). Moreover, KRC-predicted normalized variance is moderate over Valles Marineris, while Valles Marineris is typically the global maximum of A1 normalized variance. This analysis suggests that an atmospheric phenomenon dependent on roughness is a better explanation for the normalized variance distribution in A1 than inhomogenous heating/cooling of the surface being translated into heating/cooling of the lowermost atmosphere.

5.3. *Implications for gravity wave sources*

Having considered potential non-GW contributions to small-scale brightness temperature variability, it is possible to discuss the implications of this study for GW sources. Heavens et al. (2020) concluded that nadir observations by MRO-MCS generally sampled GW and mesoscale variability associated with boundary layer convection, while off-nadir observations sampled boundary layer convection as well as three other sources: (1) near the winter poles; (2) one that migrated with the winter westerly jets; and (3) one near the Equator at night during the L_s=330°–150° period.

Information from lower in the atmosphere suggests that high brightness temperature variability in tropical night is mainly dominated by the effects of mesospheric CO_2 ice clouds rather than GW activity. Analysis of A1 and A2

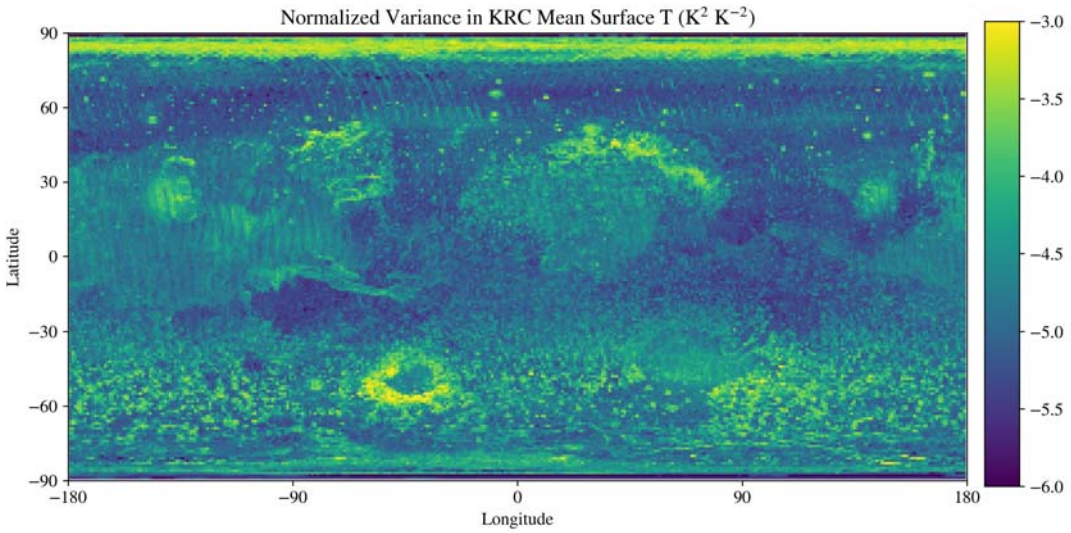

Figure 29. Normalized variance (K^2 K^{-2}) for the 20 point per degree mean surface temperature field for Mars generated by the KRC numerical thermal model (Kieffer 2013)

.

observations also somewhat weakens the reasoning behind nadir observations sampling boundary layer convection alone. Heavens et al. (2020) partly argued for boundary layer convection being sampled by nadir views on the basis of high elevation areas having higher $\hat{\Omega_{GW}}$ in A3 than low elevation and the absence of a band of high $\hat{\Omega_{GW}}$ at 50° S in dayside nadir A3 observations that was present in dayside off-nadir A3 observations. It now appears that low elevation areas like Valles Marineris have $\hat{\Omega_{GW}}$ in A1 and A2 observations, weakening the correlation between elevation and dayside $\hat{\Omega_{GW}}$ in the nadir lower in the atmosphere (Figs. 9a–b, Table 1). Moreover, there is a band of high $\hat{\Omega_{GW}}$ at 50° S in A1 and A2 dayside nadir observations that is absent in A3 (Figs. 9d–f). One argument that is robust throughout the lower atmosphere is that $\hat{\Omega_{GW}}$ is higher during the day than at night, suggesting GW activity is driven by the diurnal cycle of solar heating. This line of argument as well as the small horizontal scale of the waves sampled in the nadir argue for some contribution by boundary layer convection. Off-nadir observations suggest that the high $\hat{\Omega_{GW}}$ band at 50° S tracks the seasonal cap edge (Piqueux et al. 2015b). The disappearance of this band in A3 nadir observations but not in A3 off-nadir observations, suggests that short horizontal, large vertical wavelength GW from this source are less likely to propagate vertically than horizontally longer, vertically narrower waves. Filtering like this would imply total internal reflection of GW is common in the southern winter extratropics (Fritts & Alexander 2003).

GW activity near the winter poles is present and largely structureless at the north pole in all channels during winter (Figs. 11d,h,l) but has some embedded structures at the south pole in the winter in A1 that disappear higher in the atmosphere (Figs. 11a,e,j). The attribution of this activity to CO_2 ice clouds made by Heavens et al. (2020) remains plausible, but caution must be exercised in distinguishing variability in channels sensitive to the surface resulting from optically thick CO_2 clouds and snowfall from GW.

GW activity that migrates with the winter westerly jets probably results from a combination of weakened filtering of GW activity in the winter westerly jets (particularly on the dayside) and weaker orographic and non-orographic GW activity associated with the jets (Figs. 25a–h). These twin effects are easiest to see in northern hemisphere summer, where mid-latitude GW activity (even in rough areas) is unusually weak in A1 (Fig. 11b) and the A3/A1 activity ratio is at its minimum (Figs. 25a–h).

Yet the major new insight **provided by probing** GW activity throughout the lower atmosphere is that GW activity near the surface mostly results from orographic GW over rough surfaces. This was the initial expectation in past GCM design (Forget et al. 1999) and past observational studies (Creasey et al. 2006), but its validation with global remote sensing data is somewhat unexpected and has no parallel in GW studies at the Earth. This population, however, is largely trapped near the surface. **Orographic GW that propagate out of the lower atmosphere seem to do so in the westerly extratropical jets or easterly equatorial jet. The limited GW activity that reaches the middle atmosphere elsewhere may be non-orographic.**

6. SUMMARY

In this study, we investigated small horizontal-scale radiance variability in on-planet views by three MRO-MCS channels that sample GW activity from horizontal wavelengths < 100 km throughout most of the lower atmosphere. Our results confirm that orographic GW activity is widespread over rough areas of the planet near the surface but largely does not reach 25 km altitude outside of regions with significant jet streams. **GW activity throughout the lower atmosphere seems strongly driven by the diurnal cycle of solar heating, with dayside GW activity being generally stronger than nightside GW activity in most areas, as previously found for GW activity at 25 km by Heavens et al. (2020).**

We also demonstrate that GW activity (as measured by a quantity proportional to potential energy) decreased by a factor of 2 globally in the lower atmosphere during the planet-encircling dust event of Mars Year 34 (2018: 34P). The larger magnitude of this effect reported by Heavens et al. (2020) was biased by changing altitude sensitivity of the relevant channels under high dust opacities. The reduction of GW activity in dust storms is largely driven by suppression of near-surface GW sources by **reduced solar heating at the surface and resulting processes**, particularly in the tropics and southern extratropics. The northern extratropics was largely unaffected. But there is some evidence of reduced dissipation of GW in the tropics during this event, which may indicate stronger winds in the lower few scale heights and reduced critical level filtering.

Finally, we demonstrate that caution must be exercised when attributing all small-scale radiance variability to GW. Mesospheric clouds and significant variability in surface composition between ice and bare ground all can create small-scale radiance variability in the sampled channels and viewing geometries. It is often difficult to distinguish the signature of one of these phenomena from a poorly-resolved GW. Artifacts in this analysis resulting from mesospheric CO_2 ice cloud activity, however, may be a good proxy for GW activity at the altitude of cloud formation.

Beyond identifying areas where there is GW activity and local roughness is too low for orographic GW to occur, we have not attempted substantive investigation of non-orographic GW sources. In the case of convective sources above the boundary layer, it is difficult to confidently disentangle the GW signal from the associated clouds. Isolating potential frontal sources would require extensive image analysis and comparison with time series over smoother areas, which is well beyond the already large scope of this study. Nevertheless, the dataset derived in this study and the artifacts identified in it should be extremely useful for further investigating non-orographic sources of GW at Mars in the lower atmosphere as well as better understanding orographic GW and the conditions under which they propagate into the middle and upper atmosphere.

This work was funded by NASA's Mars Data Analysis Program (80NSSC19K1215). Work at the Jet Propulsion Laboratory, California Institute of Technology, was performed under a contract with the National Aeronautics and Space Administration. US Government sponsorship is acknowledged. Mars Climate Sounder radiance data is archived on NASA's Planetary Data System (MCS cited 2020).

The input to and results of the visibility calculations, diagnoses of variance and associated quantities, and averaged spatial fields of variance and associated quantities have been archived on Mendeley (Heavens 2021a,b). The KRC mean temperature field is available in the supporting information of Kieffer (2013).

APPENDIX

A. THE SURFACE CONTRIBUTION OVER HIGH ELEVATION SURFACES

GW variance might be erroneously diagnosed in circumstances when surface elevation or thermal inertia changes rapidly within the same observation (Heavens et al. 2020). This phenomenon arises because observations over high elevation surfaces have higher surface contributions than over low elevation surfaces (Wilson & Richardson 2000), so brightness temperatures over high elevation surfaces are sensitive to warm surface temperatures rather than the atmosphere. Mixing low and high elevation surfaces in an observation thus can produce apparently high variance in brightness temperature.

To investigate whether this effect could occur in the channels considered in this study, the relationship between brightness temperature and surface elevation in individual measurements (that is, at a detector by detector level) was studied. Data was selected within a narrow seasonal window and a small area of

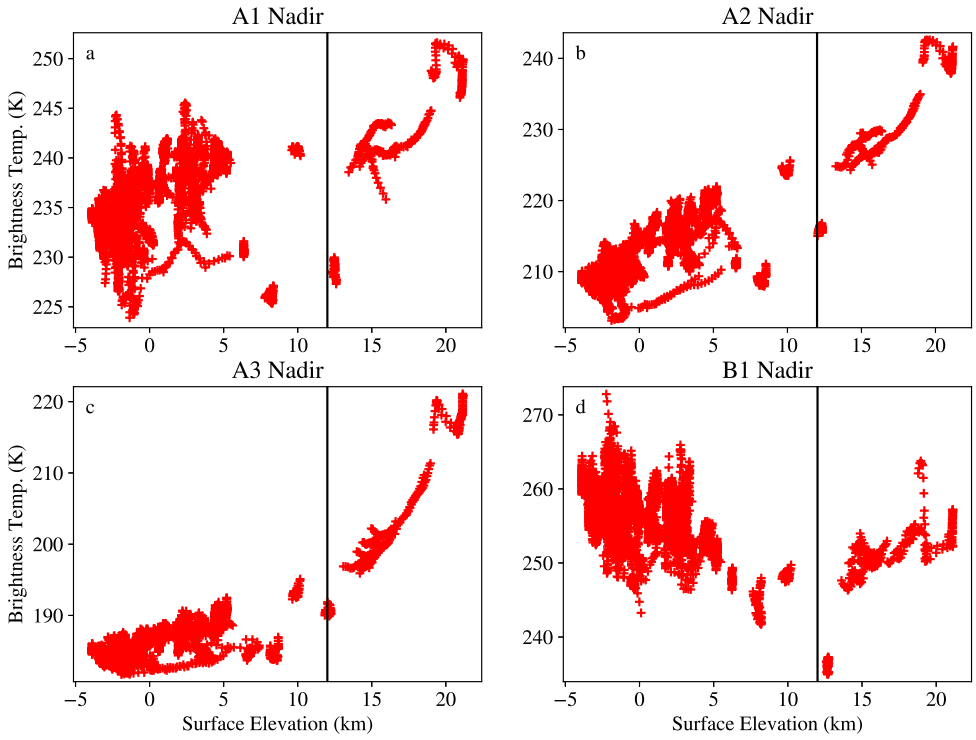

Figure A1. Surface elevation relative to Mars Orbiter Laser Altimeter (MOLA) areoid vs. brightness temperature on the dayside for nadir observations within the region of 10° S–30° N, 150°–100° W during L_s=135°–143° of MY 28 for the labeled channels. 12 km surface elevation is marked with a black vertical line. 5544 total brightness temperature measurements are plotted.

Mars with a broad range of elevations to determine if there was a critical elevation at which brightness temperatures were much higher than the typical brightness temperatures observed at low elevation, as in A.1 of Heavens et al. (2020). The main methodological change from Heavens et al. (2020) required to do this is to extend the filtering procedure based on A3 observations used in Heavens et al. (2020) to other channels. The details and consequences of this filtering procedure are discussed in Section 3.1. To get a more direct estimate of the surface contribution, we also investigated the elevation-brightness temperature relationship for the B1 channel; (290–340 cm^{-1}). B1 is used to retrieve surface temperature in MRO-MCS retrievals (Kleinböhl et al. 2011), so its brightness temperature is a reasonable approximation to surface temperature (particularly in nadir geometry), except under high aerosol conditions.

The best example of the high elevation surface contribution issue and its resolution is for A3 nadir views. (Fig. A1c). Brightness temperatures slowly increase with surface elevation, but there is considerable scatter in a range between 182 and 192 K. However, beyond 12 km surface elevation, brightness temperatures increase nearly monotonically to 220 K at 20 km surface elevation. Excluding measurements from surface elevations greater than 12 km mostly eliminates this problem.

Interpreting the additional channels is more difficult. A2 nadir views display a relation to elevation similar to A3, but brightness temperature increases faster with elevation at -5–5 km surface elevation (Fig. A1d). A1 brightness temperatures also increase with surface elevation, but the range of brightness temperatures at elevations lower than 12 km overlaps with brightness temperatures at elevations greater than 12 km (Fig. A1a). In B1 nadir views, brightness temperature actually decreases with surface elevation and its trend is mostly flat near 250 K at surface elevations between 15 and 20 km, such that brightness temperatures elevations greater than 12 km fall roughly in the middle of the range of brightness temperatures at elevations lower than 12 km (Fig. A1d). Brightness temperatures at elevations greater than 12 km in A1 and A2 trend toward 250 K, the typical brightness temperature in B1. But

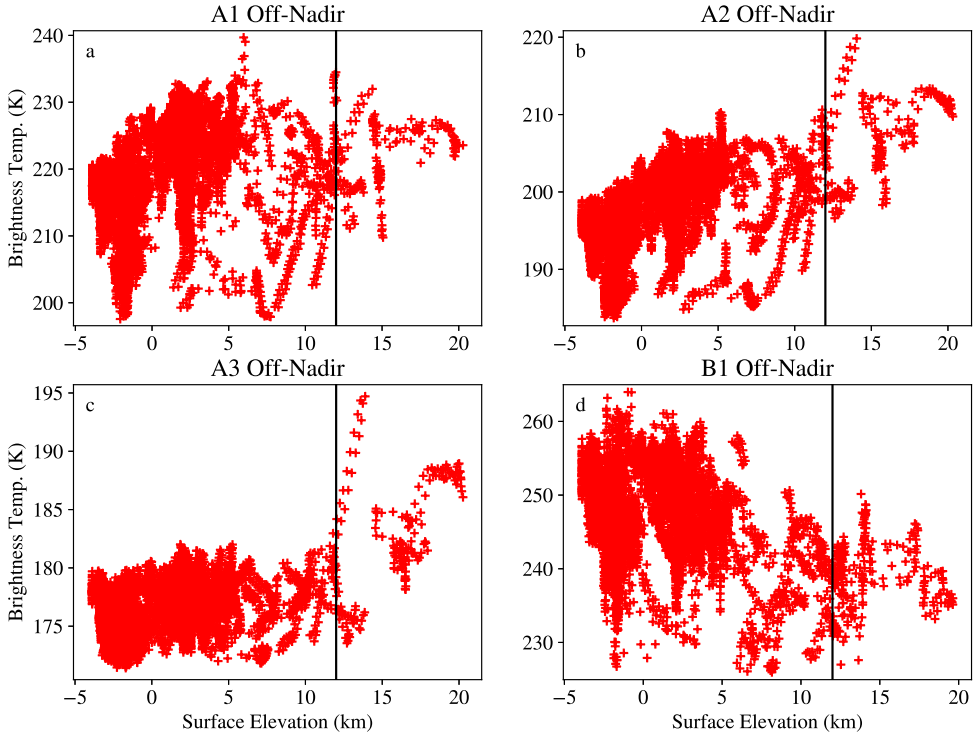

Figure A2. Surface elevation relative to Mars Orbiter Laser Altimeter (MOLA) areoid vs. brightness temperature on the dayside for off-nadir observations within the region of 10° S–30° N, 150°–100° W during L_s=135°–143° of MY 30 for the labeled channels. 12 km surface elevation is marked with a black vertical line. 7455 total brightness temperature measurements are plotted in each panel.

brightness temperatures in A1 and A2 have the opposite trend with surface elevation at elevations lower than 12 km than B1, so A1 and A2 likely observe the atmospheric temperature rather than the surface temperature at elevations lower than 12 km. The positive trend of temperature with elevation may indicate these measurements sense the convective boundary layer, whose height increases significantly with surface elevation (Hinson et al. 2008; Tellmann et al. 2013).

This analysis is little changed in the off-nadir, except that the magnitude of increases and decreases in brightness temperature with surface elevation are generally smaller and not as monotonic at high elevation (Figs. A2a–d), suggesting the surface contributions over high elevation surfaces are less of a problem than in the nadir. The one feature of interest is the rapid increase of brightness temperature with elevation near 12 km in A2, A3, and possibly A1 (Figs. A2a–c. This increase corresponds to measurements within two observations made near 20° N, 132° W, that is, around 80 km to the north of the summit of Olympus Mons. On the dayside, MCS would make these observations to the south of the surface intersection point. The horizontal weighting function of A3 in a case like this would peak around 80 km closer to the spacecraft than the intersection of the detector with the surface (see Off-Nadir_11 in Fig. 3c). Therefore, some measurements are strongly sensitive to the summit of Olympus Mons and its surface contribution at up to 21 km rather than the atmosphere/surface at 12–13 km surface elevation.

Therefore, because of the strong sensitivity of A2 and A3 nadir measurements to surface temperatures at surface elevations greater than 12 km, it seems justifiable to exclude observations at surface elevations greater than 12 km to reduce false positive diagnoses of gravity wave activity over high topography. A1, A2, and A3 off-nadir measurements seem to be less sensitive to surface temperatures at surface elevations greater than 12 km or may transition in sensitivity

at significantly greater surface elevation. However, 12 km still seems to be a reasonable criterion for exclusion because of the difficulty of registering any measurement at an exact surface elevation.

REFERENCES

Altieri, F., Spiga, A., Zasova, L., Bellucci, G., & Bibring, J.-P. 2012, J. Geophys. Res., 117, E00J08, doi: 10.1029/2012JE004065

Ando, H., Imamura, T., & Tsuda, T. 2012, J. Atmos. Sci., 69, 2906

Barnes, J. R. 1990, J. Geophys. Res., 95, 1401, doi: 10.1029/JB095iB02p01401

Battalio, M., & Wang, H. 2020, Icarus, 338, 113507, doi: https://doi.org/10.1016/j.icarus.2019.113507

Chun, H.-Y., & Kim, Y.-H. 2008, Journal of Geophysical Research: Atmospheres, 113, doi: 10.1029/2008JD009792

Clancy, R. T., Sandor, B. J., J., W. M., et al. 2000, J. Geophys. Res., 105, 9553

Clancy, R. T., Wolff, M. J., Smith, M. D., et al. 2019, Icarus, 328, 246 , doi: https://doi.org/10.1016/j.icarus.2019.03.025

Clancy, R. T., Wolff, M. J., Heavens, N. G., et al. 2021, Icarus, 362, 114411, doi: https://doi.org/10.1016/j.icarus.2021.114411

Creasey, J. E., Forbes, J. M., & Hinson, D. P. 2006, Geophys. Res. Lett., 33, L01803, doi: 10.1029/2005GL024037

DeLand, M. T., & Gorkavyi, N. 2021, J. Atmos. Sol.-Terr. Phys, 213, 105505, doi: https://doi.org/10.1016/j.jastp.2020.105505

Edwards, C. S., Nowicki, K. J., Christensen, P. R., et al. 2011, Journal of Geophysical Research: Planets, 116, doi: https://doi.org/10.1029/2010JE003755

Elrod, M. K., Bougher, S., Roeten, K., Sharrar, R., & Murphy, J. 2019, in Ninth International Conference on Mars, Pasadena, California, USA, 22-25 July 2019. https://www.hou.usra.edu/meetings/ninthmars2019/pdf/6338.pdf

Elrod, M. K., Bougher, S. W., Roeten, K., Sharrar, R., & Murphy, J. 2020, Geophysical Research Letters, 47, e2019GL084378, doi: 10.1029/2019GL084378

England, S. L., Liu, G., Yiğit, E., et al. 2017, Journal of Geophysical Research: Space Physics, 122, 2310, doi: 10.1002/2016JA023475

Ern, M., Preusse, P., Alexander, M. J., & Warner, C. D. 2004, J. Geophys. Res., 109, D20103, doi: 10.1029/2004JD004752

Forget, F., Hourdin, F., Fournier, R., et al. 1999, J. Geophys. Res., 104, 24155

Fritts, D. C., & Alexander, M. J. 2003, Rev. Geophys., 41, 3571, doi: 10.1029/2001RG000106

Fritts, D. C., Isler, J. R., Thomas, G. E., & Andreassen, Ø. 1993, Geophysical Research Letters, 20, 2039, doi: 10.1029/93GL01982

Gilli, G., Forget, F., Spiga, A., et al. 2020, Journal of Geophysical Research: Planets, 125, e2018JE005873, doi: 10.1029/2018JE005873

Guzewich, S. D., Toigo, A., & Waugh, D. 2016, Icarus, 278, 100, doi: https://doi.org/10.1016/j.icarus.2016.06.009

Guzewich, S. D., Lemmon, M., Smith, C. L., et al. 2019, Geophysical Research Letters, 46, 71, doi: 10.1029/2018GL080839

Hayne, P. O., Paige, D. A., Schofield, J. T., et al. 2012, J. Geophys. Res., 117, doi: 10.1029/2011JE004040

Heale, C. J., Bossert, K., Vadas, S. L., et al. 2020, Journal of Geophysical Research: Atmospheres, 125, e2019JD031662, doi: 10.1029/2019JD031662

Heavens, N. 2021a, Brightness Temperature Variances from On-Planet Views in the A1–A3 Channels by the Mars Climate Sounder, version 1, Mendeley, doi: http://dx.doi.org/10.17632/5k6nybdy92.1

—. 2021b, Brightness Temperature Variances from On-Planet Views in the A1–A3 and B1 Channels by the Mars Climate Sounder, version 1, Mendeley, doi: http://dx.doi.org/10.17632/y75kzcr93d.1

Heavens, N. G., Kass, D. M., Kleinböhl, A., & Schofield, J. T. 2020, Icarus, 341, 113630, doi: https://doi.org/10.1016/j.icarus.2020.113630

Heavens, N. G., Kass, D. M., & Shirley, J. H. 2019, Journal of Geophysical Research: Planets, 124, 2863, doi: 10.1029/2019JE006110

Heavens, N. G., Benson, J. L., Kass, D. M., et al. 2010, Geophysical Research Letters, 37, doi: 10.1029/2010GL044610

Hertzog, A., Boccara, G., Vincent, R. A., Vial, F., & Cocquerez, P. 2008, Journal of the Atmospheric Sciences, 65, 3056 , doi: 10.1175/2008JAS2710.1

Hinson, D. P., Pätzold, M., Tellmann, S., Häusler, B., & Tyler, G. L. 2008, Icarus, 198, 57, doi: 10.1016/j.icarus.2008.07.003

Hinson, D. P., & Wilson, R. J. 2021, Icarus, 357, 114152, doi: https://doi.org/10.1016/j.icarus.2020.114152

Holton, J. R. 1982, J. Atmos. Sci., 39, 791, doi: 10.1175/1520-0469(1982)039⟨0791:TROGWI⟩2.0.CO;2

Holton, J. R., Haynes, P. H., McIntyre, M. E., et al. 1995, Rev. Geophys., 33, 403, doi: 10.1029/95RG02097

Imamura, T., Kawasaki, Y., & Fukuhara, T. 2007, J. Atmos. Sci., 64, 1717, doi: 10.1175/JAS3914.1

Imamura, T., Watanabe, A., & Maejima, Y. 2016, Icarus, 267, 51, doi: 10.1016/j.icarus.2015.12.005

Jau, B. M., & Kass, D. 2008, in 39th Aerospace Mechanisms Symposium, Huntsville, Alabama, 7 May 2008, Citeseer, 271

Kass, D. M., Kleinböhl, A., McCleese, D. J., Schofield, J. T., & Smith, M. D. 2016, Geophys. Res. Lett., 43, 6111, doi: 10.1029/2016GL068978

Kass, D. M., Schofield, J. T., Kleinböhl, A., et al. 2020, Geophysical Research Letters, 47, e2019GL083931, doi: https://doi.org/10.1029/2019GL083931

Kieffer, H. H. 2013, Journal of Geophysical Research: Planets, 118, 451, doi: https://doi.org/10.1029/2012JE004164

Kleinböhl, A., Schofield, J., Kass, D., et al. 2010, in COSPAR Meeting, Vol. 38, 38th COSPAR Scientific Assembly, 7

Kleinböhl, A., Schofield, J. T., Abdou, W. A., Irwin, P. G. J., & de Kok, R. J. 2011, J. Quant. Spectrosc. Radiat. Transf., 112, 1568, doi: 10.1016/j.jqsrt.2011.03.006

Kleinböhl, A., Schofield, J. T., Kass, D. M., et al. 2009, J. Geophys. Res., 114, doi: 10.1029/2009JE003358

Kliore, A., ed. 1978, The Mars Reference Atmosphere (Jet Propulsion Laboratory, California Institute of Technology)

Kuroda, T., Medvedev, A. S., Yiğit, E., & Hartogh, P. 2016, J. Atmos. Sci., 73, 4895, doi: 10.1175/JAS-D-16-0142.1

Kuroda, T., Medvedev, A. S., & Yiğit, E. 2020, Journal of Geophysical Research: Planets, 125, e2020JE006556, doi: https://doi.org/10.1029/2020JE006556

Kuroda, T., Yiğit, E., & Medvedev, A. S. 2019, Journal of Geophysical Research: Planets, 124, 1618, doi: 10.1029/2018JE005847

Leelavathi, V., Venkateswara Rao, N., & Rao, S. V. B. 2020, Journal of Geophysical Research: Planets, 125, e2020JE006649, doi: https://doi.org/10.1029/2020JE006649

Lewis, S. R., Collins, M., Read, P. L., et al. 1999, Journal of Geophysical Research: Planets, 104, 24177, doi: 10.1029/1999JE001024

Listowski, C., A.Määttänen, Montmessin, F., Spiga, A., & Lefévre, F. 2014, Icarus, 237, 239, doi: https://doi.org/10.1016/j.icarus.2014.04.022

Liu, J., Jin, S., & Li, Y. 2019, Journal of Geophysical Research: Space Physics, 124, 9315, doi: 10.1029/2019JA026720

Lott, F., & Miller, M. J. 1997, Quarterly Journal of the Royal Meteorological Society, 123, 101, doi: 10.1002/qj.49712353704

Massie, S., Gille, J., Khosravi, R., et al. 2007, J. Geophys. Res. Atmospheres, 112, doi: https://doi.org/10.1029/2007JD008788

McCleese, D. J., Schofield, J. T., Taylor, F. W., et al. 2007, J. Geophys. Res., 112, doi: 10.1029/2006JE002790

MCD. cited 2018, Mars Climate Database v5.3: The Web Interface, LMD du CNRS, Paris, France

MCS. cited 2020, MRO MCS Reduced Data Records (RDR), NASA Planetary Data System Atmospheres Node, Las Cruces, NM. http://atmos.nmsu.edu/data_and_services/atmospheres_data/MARS/mcs.html

Medvedev, A. S., & Yiğit, E. 2019, Atmosphere, 10, doi: 10.3390/atmos10090531

Medvedev, A. S., Yiğit, E., Hartogh, P., & Becker, E. 2011, J. Geophys. Res., 116, E10004, doi: 10.1029/2011JE003848

Michaels, T. I., Colaprete, A., & Rafkin, S. 2006, Geophys. Res. Lett., 33, doi: 10.1029/2006GL026562

Millour, E., Forget, F., Spiga, A., et al. 2015, in European Planetary Science Conference, Vol. 10, Eur. Plan. Sci. Con. Abs. (Europlanet), 438

Minder, J. R., Mote, P. W., & Lundquist, J. D. 2010, Journal of Geophysical Research: Atmospheres, 115, doi: https://doi.org/10.1029/2009JD013493

Montabone, L., Spiga, A., Kass, D. M., et al. 2020, Journal of Geophysical Research: Planets, 125, e2019JE006111, doi: https://doi.org/10.1029/2019JE006111

Offermann, D., Jarisch, M., Oberheide, J., et al. 2006, Journal of Atmospheric and Solar-Terrestrial Physics, 68, 1709 , doi: https://doi.org/10.1016/j.jastp.2006.01.013

Palmer, T. N., Shutts, G. J., & Swinbank, R. 1986, Quarterly Journal of the Royal Meteorological Society, 112, 1001, doi: 10.1002/qj.49711247406

Parish, H. F., Schubert, G., Hickey, M. P., & Walterscheid, R. L. 2009, Icarus, 203, 28, doi: 10.1016/j.icarus.2009.04.031

Pepin, N. C., Maeda, E. E., & Williams, R. 2016, Journal of Geophysical Research: Atmospheres, 121, 9998, doi: https://doi.org/10.1002/2016JD025497

Piqueux, S., Byrne, S., Kieffer, H. H., Titus, T., & Hansen, C. J. 2015a, Icarus, 251, 332, doi: 10.1016/j.icarus.2014.12.014

Piqueux, S., Edwards, C. S., & Christensen, P. R. 2008, Journal of Geophysical Research: Planets, 113, doi: https://doi.org/10.1029/2007JE003055

Piqueux, S., Kleinböhl, A., Hayne, P. O., et al. 2015b, Icarus, 251, 164 , doi: 10.1016/j.icarus.2014.10.045

Rafkin, S. C. R., & Michaels, T. I. 2003, Journal of Geophysical Research: Planets, 108, doi: https://doi.org/10.1029/2002JE002027

Rafkin, S. C. R., Sta. Maria, M. R. V., & Michaels, T. I. 2002, Nature, 419, 697, doi: 10.1038/nature01114

Rajendran, K., Lewis, S. R., Holmes, J. A., et al. 2021, Geophysical Research Letters, 48, e2021GL094634, doi: https://doi.org/10.1029/2021GL094634

Sefton-Nash, E., Teanby, N., Montabone, L., et al. 2013, Icarus, 222, 342 , doi: https://doi.org/10.1016/j.icarus.2012.11.012

Shirley, J. H., Kleinböhl, A., Kass, D. M., et al. 2020, Geophysical Research Letters, 47, e2019GL084317, doi: 10.1029/2019GL084317

Siddle, A., Mueller-Wodarg, I., Stone, S., & Yelle, R. 2019, Icarus, 333, 12 , doi: https://doi.org/10.1016/j.icarus.2019.05.021

Slipski, M., Jakosky, B. M., Benna, M., et al. 2018, Journal of Geophysical Research: Planets, 123, 2939, doi: 10.1029/2018JE005704

Smith, D., Neumann, G., Arvidson, R. E., Guinness, E. A., & Slavney, S. 2003, Mars Global Surveyor Laser Altimeter Mission Experiment Gridded Data Record: MGS-M-MOLA-5-MEGDR-L3-V1.0, NASA Planetary Data System Geosciences Node, St, Louis, MO

Spiga, A. 2011, Plan. Space Sci., 59, 915, doi: 10.1016/j.pss.2010.04.025

Spiga, A., González-Galindo, F., López-Valverde, M. Á., & Forget, F. 2012, Geophys. Res. Lett., 39, L02201, doi: 10.1029/2011GL050343

Spiga, A., Hinson, D. P., Madeleine, J.-B., et al. 2017, Nature Geoscience, 10, 652, doi: 10.1038/ngeo3008

Tellmann, S., Pätzold, M., Häusler, B., Hinson, D. P., & Tyler, G. L. 2013, J. Geophys. Res., 118, 306, doi: 10.1002/jgre.20058

Titus, T. N., Kieffer, H. H., & Christensen, P. R. 2003, Science, 299, 1048, doi: 10.1126/science.1080497

Toigo, A. D., & Richardson, M. I. 2002, J. Geophys. Res., 107, 5049, doi: 10.1029/2000JE001489

Vadas, S. L., & Fritts, D. C. 2001, Journal of the Atmospheric Sciences, 58, 2249, doi: 10.1175/1520-0469(2001)058⟨2249:GWRAMR⟩2.0.CO;2

Vadas, S. L., Zhao, J., Chu, X., & Becker, E. 2018, Journal of Geophysical Research: Atmospheres, 123, 9296, doi: https://doi.org/10.1029/2017JD027970

Vals, M., Spiga, A., Forget, F., et al. 2019, Planetary and Space Science, 178, 104708, doi: 10.1016/j.pss.2019.104708

Walterscheid, R. L., Hickey, M. P., & Schubert, G. 2013, Journal of Geophysical Research (Planets), 118, 2413, doi: 10.1002/jgre.20164

Wang, H. 2007, Icarus, 189, 325, doi: 10.1016/j.icarus.2007.01.014

Williamson, H. N., Johnson, R. E., Leclercq, L., & Elrod, M. K. 2019, Icarus, 331, 110 , doi: https://doi.org/10.1016/j.icarus.2019.05.020

Wilson, R. J. 1997, Geophys. Res. Lett., 24, 123, doi: 10.1029/1996GL03814

Wilson, R. J., & Richardson, M. I. 2000, Icarus, 145, 555, doi: 10.1006/icar.2000.6378

Wolff, M. J., & Clancy, R. T. 2003, Journal of Geophysical Research: Planets, 108, doi: 10.1029/2003JE002057

Wright, C. J., Osprey, S. M., & Gille, J. C. 2013, Journal of Geophysical Research: Atmospheres, 118, 10,980, doi: 10.1002/jgrd.50869

Wu, D. L., & Eckermann, S. D. 2008, J. Atmos. Sci., 65, 3695, doi: 10.1175/2008JAS2489.1

Wu, D. L., Preusse, P., Eckermann, S. D., et al. 2006, Adv. Space. Res., 37, 2269, doi: 10.1016/j.asr.2005.07.031

Xu, S., Liemohn, M., Bougher, S., & Mitchell, D. 2015, Geophysical Research Letters, 42, 9702, doi: 10.1002/2015GL066043

Yamanaka, M. 1995, Adv. Space. Res., 15, 47 , doi: https://doi.org/10.1016/0273-1177(94)00063-7

Yiğit, E., England, S. L., Liu, G., et al. 2015, Geophysical Research Letters, 42, 8993, doi: 10.1002/2015GL065307

Yiğit, E., & Medvedev, A. S. 2015, Advances in Space Research, 55, 983 , doi: https://doi.org/10.1016/j.asr.2014.11.020

Yiğit, E., Medvedev, A. S., Benna, M., & Jakosky, B. M. 2020, Geophysical Research Letters, n/a, e2020GL092095, doi: https://doi.org/10.1029/2020GL092095

Yiğit, E., Medvedev, A. S., & Hartogh, P. 2018, Annales Geophysicae, 36, 1631, doi: 10.5194/angeo-36-1631-2018